

On the dissection of degenerate cosmologies with machine learning

Julian Merten,¹★ Carlo Giocoli,^{1,2,3,4} Marco Baldi,^{1,3,4} Massimo Meneghetti,^{1,3,4} Austin Peel,⁵ Florian Lalande,^{5,6} Jean-Luc Starck,⁵ and Valeria Pettorino⁵

¹INAF-Osservatorio di Astrofisica e Scienza dello Spazio di Bologna, Via Gobetti 93/3, 40129, Bologna, Italy

²Dipartimento di Fisica e Scienze della Terra, Università degli Studi di Ferrara, via Saragat 1, I-44122 Ferrara, Italy

³Dipartimento di Fisica e Astronomia, Alma Mater Studiorum Università di Bologna, via Gobetti 93/2, I-40129 Bologna, Italy

⁴INFN – Sezione di Bologna, viale Berti Pichat 6/2, I-40127 Bologna, Italy

⁵AIM, CEA, CNRS, Université Paris-Saclay, Université Paris Diderot, Sorbonne Paris Cité, F-91191 Gif-sur-Yvette, France

⁶ENSAI, rue Blaise Pascal, 35170 Bruz, France

© 2018 INAF. All rights reserved.

Accepted for publication by the Monthly Notices of the Astronomical Society.

ABSTRACT

Based on the DUSTGRAIN-*pathfinder* suite of simulations, we investigate observational degeneracies between nine models of modified gravity and massive neutrinos. Three types of machine learning techniques are tested for their ability to discriminate lensing convergence maps by extracting dimensional reduced representations of the data. Classical map descriptors such as the power spectrum, peak counts and Minkowski functionals are combined into a joint feature vector and compared to the descriptors and statistics that are common to the field of digital image processing. To learn new features directly from the data we use a Convolutional Neural Network (CNN). For the mapping between feature vectors and the predictions of their underlying model, we implement two different classifiers; one based on a nearest-neighbour search and one that is based on a fully connected neural network.

We find that the neural network provides a much more robust classification than the nearest-neighbour approach and that the CNN provides the most discriminating representation of the data. It achieves the cleanest separation between the different models and the highest classification success rate of 59% for a single source redshift. Once we perform a tomographic CNN analysis, the total classification accuracy increases significantly to 76% with no observational degeneracies remaining. Visualising the filter responses of the CNN at different network depths provides us with the unique opportunity to learn from very complex models and to understand better why they perform so well.

Key words: gravitation – neutrinos – large-scale structure of Universe – methods: numerical

1 INTRODUCTION

The standard Λ CDM cosmological model – based on a cosmological constant as the source of the observed accelerated cosmic expansion (Riess et al. 1998; Perlmutter et al. 1999; Schmidt et al. 1998) and on cold dark matter particles as the bulk of the clustering mass in the universe (White & Rees 1978; White 1993, 1996; Springel et al. 2005) – has survived the past two decades of cosmological observations targeted to a wide range of independent probes. This includes the statistical properties of Cosmic Microwave Background (CMB)

anisotropies (Bennett et al. 2013; Planck Collaboration et al. 2018), the large-scale distribution and dynamics of visible galaxies (Parkinson et al. 2012; Alam et al. 2017; Pezzotta et al. 2017), weak gravitational lensing signals (Fu et al. 2008; Joudaki et al. 2017; Hildebrandt et al. 2017; Troxel et al. 2018; Hikage et al. 2018), the abundance of galaxy clusters, as well as its time evolution (Vikhlinin et al. 2009; Planck Collaboration et al. 2016b).

Despite this astonishing success, the fundamental nature of the two main ingredients of the Λ CDM model – summing up to about 95% of the total energy density of the universe – remains unknown. On one side, the energy scale associated with the cosmological constant does not

* E-mail: julian.merten@inaf.it

find any reasonable explanation in the context of fundamental physics, with predictions based on the standard model of particle physics failing by tens of orders of magnitude. On the other hand, no clear detection – direct or indirect – of any new fundamental particle that may be associated with cold dark matter has been made despite a longstanding chase through astrophysical observations (Aartsen et al. 2013; Ackermann et al. 2017; Albert et al. 2017) and laboratory experiments (see e.g. Bernabei et al. 2018; ATLAS Collaboration 2013; CMS Collaboration 2016).

This leaves the next generation of cosmological observations with the arduous challenge of clarifying the fundamental nature of the dark sector by systematically scrutinising the huge wealth of high-quality data that will be made available in the near future by several wide-field surveys (such as Laureijs et al. 2011; Ivezić et al. 2008; Spergel et al. 2015; Benítez et al. 2014). As a matter of fact, any possible insights from future datasets must come in the form of very small deviations from the expectations of the Λ CDM model, otherwise past observations would have already detected them. This suggests that either the fundamental physics behind dark energy and dark matter is indeed extremely close to that of General Relativity (GR) with a cosmological constant and heavy fundamental particles with negligible thermal velocities, respectively, or that a more radical shift from this standard paradigm is hidden and masked by other effects such as an observational degeneracy with some not yet fully constrained cosmological parameter. The latter scenario may result in a severe limitation of the discriminating power of observations, thereby providing a particularly challenging testbed for the next generation of cosmological surveys.

A typical example of such a possible intriguing situation is given by the well-known degeneracy between some Modified Gravity (MG, see e.g. Amendola et al. 2018, for a recent review on a wide range of MG scenarios) theories and the yet unknown value of the neutrino mass. It is now generally accepted (Baldi et al. 2014; He 2013; Motohashi et al. 2013; Wright et al. 2017) that MG theories such as $f(R)$ gravity (Buchdahl 1970) are strongly observationally degenerate with the effects of massive neutrinos on structure formation (see Baldi et al. 2014). Some commonly adopted statistics such as the matter auto-power spectrum (Giocoli et al. 2018a), the lensing convergence power spectrum (Peel et al. 2018), and the halo mass function (Hagstotz et al. 2018) may hardly distinguish standard Λ CDM expectations from some specific combinations of the $f(R)$ gravity parameters and the total neutrino mass.

As such degeneracies extend down to the non-linear regime of structure formation, the use of full numerical simulations currently represents the only viable method to explore these scenarios, even though alternative approaches based on approximate methods (see e.g. Wright et al. 2017) have been developed in the last years and are being tested and calibrated against simulations. In the present work, we will explore the prospects of using machine learning techniques applied to numerical simulations of both MG and Λ CDM cosmologies that are highly observationally degenerate through standard observational statistics.

Several variants of higher-order statistics have been applied in the past to characterise cosmological data sensitive to the late-time evolution of structure in the Universe.

Recent analyses of the weak lensing (WL) (Bartelmann & Schneider 2001) data from CFHTLens (Heymans et al. 2012) used either higher-order (>2) moments of the convergence field (Van Waerbeke et al. 2013), or Minkowski functionals (Petri et al. 2015) to draw cosmological inference from a data description that goes beyond two-point statistics. Martinet et al. (2018) and Shan et al. (2018) applied peak count statistics (Dietrich & Hartlap 2010; Kratochvil et al. 2010) to shear and convergence fields from KiDS (Hildebrandt et al. 2017) and Gruen et al. (2018) used counts-in-cells (Friedrich et al. 2018) to extract information from the DES (Abbott et al. 2018) catalogues. A new set of techniques based on deep learning (LeCun et al. 2015) currently has gained momentum in many scientific fields, including astrophysics. The extremely complex models which can be constructed through a modular building-block concept (e.g. Chollet 2017) have been very successful for tasks like language translation (e.g. Wu et al. 2016; Johnson et al. 2016), text and handwriting recognition (e.g. Graves 2013), as well as for the classification of images (starting with the seminal work of Krizhevsky et al. 2012). In cosmology, deep learning is used for the extraction of information from N-body simulations (Ravanbakhsh et al. 2017), to learn the connection between initial conditions and the final shape of structure (Lucie-Smith et al. 2018), for the characterisation of point spread functions (Herbel et al. 2018) or the measurement of shear for WL (Springer et al. 2018), the characterisation of non-Gaussian structure in mass maps (Gupta et al. 2018), the determination of galaxy cluster X-ray masses (Ntampaka et al. 2018) and the fast creation of simulated data using generative adversarial networks (Rodriguez et al. 2018). In this work, we will use such techniques to break the degeneracies between models of modified gravity in the presence of massive neutrinos.

The text is organised as follows: Section 2 gives an overview of the numerical simulations and the creation of the mass maps that constitute our main data set. In section 3 we introduce the different characterisation and classification techniques that we apply to the mass map data and show the results that they produce in section 4. We present our conclusions in section 5. Two appendices provide more details on certain technical aspects of the computer vision (appendix A) and deep neural network (appendix B) methods we are using.

2 NUMERICAL SIMULATIONS

We perform our analysis on a set of WL maps extracted from a suite of cosmological dark matter-only simulations called the DUSTGRAIN-*pathfinder* runs. These simulations represent a preliminary calibration sample for the DUSTGRAIN (Dark Universe Simulations to Test GRAvity In the presence of Neutrinos) project, an ongoing numerical effort aimed at investigating cosmological models characterised by a modification of the laws of gravity from their standard GR form and by a non-negligible fraction of the cosmic matter density being made of standard massive neutrinos.

2.1 DUSTGRAIN-*pathfinder*

The modification of gravity considered in the DUSTGRAIN project consists in an $f(R)$ model defined by the Action (Buchdahl 1970)

$$S = \int d^4x \sqrt{-g} \left(\frac{R + f(R)}{16\pi G} + \mathcal{L}_m \right). \quad (1)$$

We assume a specific analytical form for the $f(R)$ function (Hu & Sawicki 2007)

$$f(R) = -m^2 \frac{c_1 \left(\frac{R}{m^2} \right)^n}{c_2 \left(\frac{R}{m^2} \right)^n + 1}, \quad (2)$$

where R is the Ricci scalar curvature, $m^2 \equiv H_0^2 \Omega_M$ is a mass scale, while $\{c_1, c_2, n\} \geq 0$ are free parameters of the model. Such a form is particularly popular and widely investigated as it allows one to recover with arbitrary precision a Λ CDM background expansion history by choosing $c_1/c_2 = 6\Omega_\Lambda/\Omega_M$. Here Ω_Λ and Ω_M are the vacuum and matter energy density, respectively, under the condition $c_2(R/m^2)^n \gg 1$, so that the scalar field f_R takes the approximate form

$$f_R \approx -n \frac{c_1}{c_2^2} \left(\frac{m^2}{R} \right)^{n+1}. \quad (3)$$

By restricting to the case $n = 1$ the only remaining free parameter of the model can be written as

$$f_{R0} \equiv -\frac{1}{c_2} \frac{6\Omega_\Lambda}{\Omega_M} \left(\frac{m^2}{R_0} \right)^2 \quad (4)$$

and its absolute value $|f_{R0}|$ will quantify how much the model departs from GR.

The DUSTGRAIN-*pathfinder* simulations have been devised to sample the $\{f_{R0}, m_\nu\}$ parameter space and to identify highly degenerate combinations of parameters. Some analyses of the corresponding WL signal have been presented by Giocoli et al. (2018a) and Peel et al. (2018), while Hagstotz et al. (2018) have used the simulations to calibrate a theoretical modelling of the halo mass function in $f(R)$ gravity with and without the contribution of massive neutrinos. In this further paper, we will use machine learning techniques to tackle the issue of observational degeneracy in these combined models based on the WL reconstruction described in Giocoli et al. (2018a). A similar approach, focused on a subset of particularly degenerate models is presented in Peel et al. (2018b, PRL submitted).

From a technical point of view, the DUSTGRAIN-*pathfinder* runs are cosmological collisionless simulations including 768^3 Dark Matter particles of mass $m_{\text{CDM}} = 8.1 \times 10^{10} M_\odot/h$ (for the case of $m_\nu = 0$) and as many neutrino particles (for the case of $m_\nu > 0$) in a $(750 \text{Mpc}/h)^3$ cosmological volume with periodic boundary conditions evolving under the effect of a gravitational interaction defined by equation 1. The simulations have been performed with the MG-GADGET code (see Puchwein et al. 2013), a modified version of the GADGET code (Springel 2005) that implements all the modifications that characterise $f(R)$ gravity (see Puchwein et al. 2013, for more details on the algorithm). MG-GADGET has been extensively tested (see e.g. the Modified Gravity code comparison project described in Winther et al. 2015) and employed recently for a wide variety of applications (Baldi & Villaescusa-Navarro 2018; Arnold et al. 2018,

2014; Arnold et al. 2015; Roncarelli et al. 2018; Arnold et al. 2016; Naik et al. 2018). For the DUSTGRAIN-*pathfinder* simulations, as was already done in Baldi et al. (2014), we have combined the MG-GADGET solver with the particle-based implementation of massive neutrinos developed by Viel et al. (2010). This allowed us to include massive neutrinos in the simulations as an independent family of particles with its own initial transfer function and velocity distribution. Initial conditions have been generated following the approach of e.g. Zennaro et al. (2017) and Villaescusa-Navarro et al. (2017) at the starting redshift of the simulation $z_i = 99$ with thermal neutrino velocities added on top of the gravitational velocities by random sampling the neutrino momentum distribution at the initial redshift.

Standard cosmological parameters are set to be consistent with the Planck 2015 constraints (Planck Collaboration et al. 2016a). Concerning non-standard parameters, the DUSTGRAIN-*pathfinder* simulations spanned the range $-1 \times 10^{-4} \leq f_{R0} \leq -1 \times 10^{-6}$ for the scalar amplitude and $0 \text{ eV} \leq m_\nu \leq 0.3 \text{ eV}$ for the neutrino mass, for a total of 20 simulations. In the present work, we will consider a subset of the full DUSTGRAIN-*pathfinder* suite consisting of nine simulations whose specifications are summarised in table 1.

2.2 Lensing light-cones

For all simulations we stored 34 snapshots at different redshifts that allow us to construct lensing light-cones up to a source redshift $z_s = 4$ without gaps. Different methods have been developed to produce lensing light-cones from large cosmological N-body simulations. Recent works have employed post-processing reconstructions based on the slicing of a set of comoving particle snapshots (as e.g. in Hilbert et al. 2008, 2009; Giocoli et al. 2016; Shirasaki et al. 2017), as well as on-the-fly algorithms capable of storing only the projected matter density on a given field-of-view without resorting on the flat-sky approximation (see e.g. Barreira et al. 2016; Arnold et al. 2018). In this work we use the MAPSIM routine (Giocoli et al. 2014; Tessore et al. 2015; Castro et al. 2018) which is based on the former strategy. We use the particles stored in 21 different snapshots to construct our continuous past-light-cones up to $z = 4$, building 27 lens planes of the projected matter density distribution, considering a square sky coverage of five degrees on a side. For each cosmological model we construct 256 different light-cone realisations by randomising the various comoving cosmological boxes (Giocoli et al. 2018a; Peel et al. 2018).

2.3 Convergence maps

The MAPSIM pipeline is composed of two algorithms. The first one – called i-MAPSIM – constructs lensing planes from the different simulation snapshots, saving for each plane l and on each pixel with coordinate indices (i, j) the particle surface mass density Σ

$$\Sigma_l(i, j) = \frac{\sum_k m_k}{A_l}. \quad (5)$$

A_l represents the comoving pixel area of the lens plane l and $\sum_k m_k$ the sum over all particle masses associated with the given pixel. The second algorithm named ray-MAPSIM

Simulation Name	Gravity type	f_{R0}	m_ν [eV]	Ω_{CDM}	Ω_ν	m_{CDM}^P [M_\odot/h]	m_ν^P [M_\odot/h]
ΛCDM	GR	–	0	0.31345	0	8.1×10^{10}	0
f_4	$f(R)$	-1×10^{-4}	0	0.31345	0	8.1×10^{10}	0
f_5	$f(R)$	-1×10^{-5}	0	0.31345	0	8.1×10^{10}	0
f_6	$f(R)$	-1×10^{-6}	0	0.31345	0	8.1×10^{10}	0
$f_4^{0.3}$	$f(R)$	-1×10^{-4}	0.3	0.30630	0.00715	7.92×10^{10}	1.85×10^9
$f_5^{0.15}$	$f(R)$	-1×10^{-5}	0.15	0.30987	0.00358	8.01×10^{10}	9.25×10^8
$f_5^{0.1}$	$f(R)$	-1×10^{-5}	0.1	0.31107	0.00238	8.04×10^{10}	6.16×10^8
$f_6^{0.1}$	$f(R)$	-1×10^{-6}	0.1	0.31107	0.00238	8.04×10^{10}	6.16×10^8
$f_6^{0.06}$	$f(R)$	-1×10^{-6}	0.06	0.31202	0.00143	8.07×10^{10}	3.7×10^8

Table 1. The subset of the DUSTGRAIN-*pathfinder* simulations considered in this work with their specific parameters. f_{R0} represents the MG parameter, m_ν and m_ν^P the neutrino mass in electron volts and in M_\odot/h as implemented in the simulation, m_{CDM}^P cold dark matter particle mass, and Ω_{CDM} and Ω_ν the CDM and neutrino density parameters, respectively.

projects the matter density distribution along the line-of-sight by weighing the lens planes with the lensing kernel in the Born approximation regime (Bartelmann & Schneider 2001; Schäfer et al. 2012; Petri 2016; Giocoli et al. 2016; Petri et al. 2017; Giocoli et al. 2017, 2018b; Castro et al. 2018). From Σ_l we can derive the convergence κ at a given source redshift z_s as

$$\kappa = \sum_l \frac{\Sigma_l}{\Sigma_{\text{crit},l,s}}, \quad (6)$$

where l varies over the different lens planes with the lens redshift z_l smaller than z_s and $\Sigma_{\text{crit},l,s}$ represents the critical surface density at the lens plane z_l for sources at redshift z_s

$$\Sigma_{\text{crit},l,s} \equiv \frac{c^2}{4\pi G} \frac{D_l}{D_s D_{ls}}. \quad (7)$$

Here c is the speed of light, G is Newton’s constant and D_l , D_s and D_{ls} are the angular diameter distances between observer-lens, observer-source and source-lens, respectively. The final κ maps cover the 25 square degree field-of-view with 2048^2 pixels, resulting in a map resolution of ~ 8.8 arcseconds.

3 METHODOLOGY

A variety of machine learning techniques is applied to the DUSTGRAIN-*pathfinder* convergence maps. It was shown by Peel et al. (2018) that summary statistics up to second-order do not reliably separate such mass maps. Higher-order statistics, especially peak counts (e.g. Peel et al. 2017; Shan et al. 2018; Martinet et al. 2018; Lin & Kilbinger 2018), do a better job but still leave room for improvement when distinguishing between a large number of models and in the presence of noise. Most commonly used methods to characterise observational data are naturally based on physical models. In the following we present an agnostic approach, which also applies techniques and algorithms found in the fields of computer science and specifically digital image processing.

We distinguish two subsequent steps in the process of mass map classification. The first is to find a feature extraction function Θ , which takes a high-dimensional data vector

x as input and finds a general, dimensional reduced representation of it in the form of a feature vector F

$$\Theta(x; w_f) = F. \quad (8)$$

The feature extraction function can have several parameters which are stored in the feature weight vector w_f . In order to arrange the data vector x in a meaningful way, we introduce an index notation x_{ijc} . The first two indices reflect a spatial ordering of the 2D data along the coordinate axes. This means that all elements with $i = 1$ are located in the first row of the pixelised image and all elements with e.g. $j = 10$ are located in the tenth column of the image. This notation also includes 1D data, ordered or not, by setting $i = 1 \forall j, c$. The third index c –commonly dubbed as a channel– allows us to collect multiple aspects of the same entity represented by x . For the example of an RGB-image, $c = 1$ would be the red channel of the image, $c = 2$ the green and $c = 3$ the blue channel. Finally, we define the shape of a data vector with a bracket notation. The shape of our input convergence maps is $\#x = (2048, 2048, 6)$ since we have 2048×2048 pixel maps with convergence values κ at six different source redshift channels and where in the above we have introduced the shape operator $\#$ which returns the shape of a data vector.

The second step classifies F into a set of target classes. The classification function ζ , which can again depend on a set of parameters w_m , should not only output a single class prediction, but rather a prediction vector P of shape $\#P = (1, 1, n)$ with probabilities to belong to each of n target classes

$$\zeta(F, w_m) = P. \quad (9)$$

It must hold that $P_n \in [0, 1]$, $\sum P_n = 1$ and in our case $n \in (1, \dots, 9)$.

In the following we explore different choices for the feature extraction and classification functions and find ways to optimise their parameters to achieve an optimal classification. We do so with the help of training sets, which are data vector–label pairs (x, y^l) , meaning mass maps for which we a-priori know the underlying cosmological model. Specifically, the label y^l is an indicator function for the class $l \in (1, \dots, 9)$ with elements y_k^l for which

$$y_k^l = \begin{cases} 1 & \text{if } k = l \\ 0 & \text{else.} \end{cases} \quad (10)$$

3.1 Definition of data sets

Our full data set consists of 256 convergence maps of shape (2048,2048,6) for each of the nine cosmological models. We split each map further into 64 smaller patches to define our main data vectors with $\#x = (256, 256, 6)$. 75% of those maps (12289) are used as a training set in order to optimise the parameters of our models. We use 15% of the maps (2457) as a validation set where the correct labels y are known to us, but not to the optimisation algorithm. Performing a classification on the validation data serves as quality control and helps us to decide if an optimisation is successful and when to stop it. Another 10% of the maps (1638) are used as a test set, where the labels are not known to us a-priori and to which our trained and validated algorithms are applied to blindly. The success rates on those test sets will be the main result of this work. We provide examples of the actual data in the left panel of figure 1, which shows example convergence maps, chosen at random from the test set, for four instructive models. This includes the Λ CDM reference, f_4 which deviates most from Λ CDM, $f_6^{0.06}$ which is observationally most degenerate with Λ CDM and a sample map of $f_5^{0.1}$ which is between the two extremes. The source redshift for all the maps shown is $z_s = 1.0$.

3.2 Mass map feature extraction

Two important subclasses for Θ are possible. In the first, the parameters w_f are free and can be optimised during a training phase. In the second, they are fixed. We want to highlight that we do not perform any initial transformations of the data, which have proven to be useful for the analysis of lensing mass maps. It was shown in e.g. Peel et al. (2018) that an aperture mass transformation (Schneider 1996; Schneider et al. 1998) can largely improve the discrimination power of certain statistics, but we want to stay as general and agnostic as possible at this stage and use the raw pixel data of the convergence maps as the initial data vector.

3.2.1 Standard mass map descriptors

Examples of fixed feature extraction are the mass map descriptors which are commonly used in the cosmological community to describe convergence or shear catalogues. For the purposes of this work, such descriptors serve as the reference for other techniques that we apply. We combine a number of mass map features, which we extract with the `LensTools` package¹ by Petri (2016) into a feature vector of shape (1,1,99). The first four entries in this vector are the mean, variance, skewness and kurtosis of the convergence maps. This is followed by eleven percentiles between the 0th-percentile (the minimum) and the 100th-percentile (the maximum) in steps of ten percent. The normalised histogram (PDF) of the convergence values in each map is sorted with 14 bins and the value for each bin is appended to the feature vector. Next, we calculate the power spectrum in 14 logarithmically spaced bins between $l = 1000$ and $l = 32000$, which cover the angular size and resolution of our mass maps. Finally, we use the standard deviation of

each map to define 14 signal-to-noise bins between -2 and 5. For each such bin we calculate the peak counts, as well as the first three Minkowski functionals (e.g. Kratochvil et al. 2012; Petri et al. 2015, and references therein), which concludes our collection of 99 features. The right panel of figure 1 shows examples for the variation between models for such classical features. Presented there is the average power spectrum and peak count for all maps in the test set and for the four instructive models we chose in section 3.1 for data visualisation purposes.

3.2.2 Classical computer vision

We know from Peel et al. (2018) that at least some of the standard descriptors above are not optimally suited for the task at hand and it is, at this point, not entirely obvious how to define better ones. This is why we now aim to derive as many fixed features as possible. The publicly available `wnd-charm` algorithm (Shamir et al. 2008; Orlov et al. 2008; Shamir et al. 2010) was designed for the classification of microscopy images and derives a particularly large feature vector of shape (1,1,2919). This includes most of the common statistics and descriptors known to digital image processing. Many features are thereby not only calculated from the raw image, but from some of its alternative representations like the Fourier, Wavelet, Chebyshev or Edge transformation. Moreover, some features are also extracted from transformations of transformations. While we did state earlier that we do not want to yet our data with transformations, we want to point out that the listed transformations are by no means inspired by the mechanisms of lensing or structure formation. We refer the interested reader to Orlov et al. (2008) for the full description of the algorithm and the description of the full feature vector, but we do provide a short summary in appendix A and a compact overview in table A1.

3.2.3 Convolutional neural networks

As the class of feature extraction functions which are able to change their shape during the training process we chose multi-layered neural networks (LeCun et al. 2015; Goodfellow et al. 2016). The input data vector x is manipulated and eventually reduced in dimension by a long –deep– chain of simple layers θ , which implement a specific mathematical operation. The output of one layer, becomes the input of the following layer and contains its own set of parameters w_i . The set of all layer parameters becomes the feature parameter vector w_f .

$$\Theta(x, w_f) = \theta_n \circ \theta_{n-1} \circ \dots \circ \theta_1 \quad (11)$$

$$\theta_i \circ \theta_{i-1}(\cdot) \equiv \theta_i(\theta_{i-1}(\cdot, w_{i-1}), w_i) \quad (12)$$

$$w_f \equiv \{w_i\}_{i=1}^n \quad (13)$$

Deep neural networks source their performance from the sheer number of layers they are comprised of and have gained much popularity in recent years. This is mainly due to the advancements in numerical performance by e.g. exploiting many-core architectures². This allows for the construction

¹ <https://github.com/apetri/LensTools>

² General Purpose Graphics Processing Units (GPGPU) are a popular example of a many-core architecture.

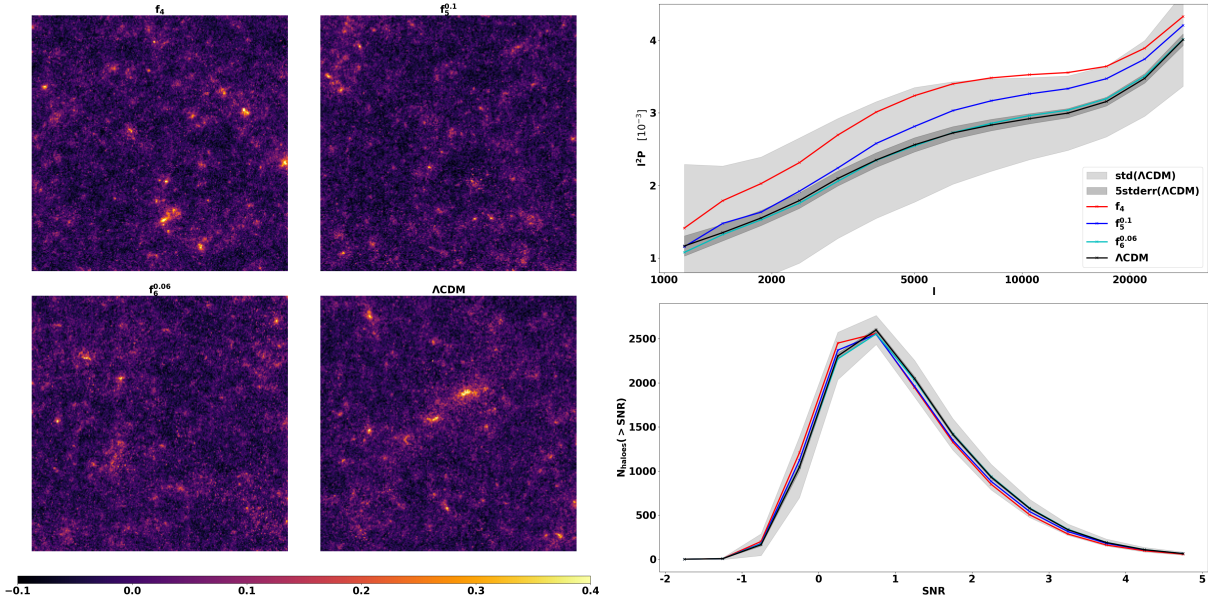


Figure 1. The *left panel* shows randomly chosen convergence maps from the test set in four specifically chosen models of structure formation. Those models span the range of observational degeneracy from the ΛCDM reference, with f_4 being the most distinct, $f_6^{0.06}$ the most similar and $f_5^{0.1}$ the middle ground between the extremes. The *right panel* shows, for the same models, the average power spectrum over all maps in the test set on the *top* and the peak counts as a function of signal-to-noise on the *bottom*. The coloured lines indicate the results for the four different models, while the grey shaded areas indicate typical variations within the test set sample for the case of ΛCDM . The source redshift in all cases is $z_s = 1.0$.

of particularly deep and complex networks with hundreds of millions of parameters. The functional forms of the layers that are used in a deep neural network depend on the problem at hand. For image classification, convolutional neural networks (CNN) have proven to be particularly useful (Krizhevsky et al. 2012; Simonyan & Zisserman 2014; Szegedy et al. 2014; He et al. 2015; Lin et al. 2017) and hence we chose this class of models for our purposes. The main functionality of a CNN is provided by a convolutional layer $\text{Conv}(n, m, \Delta i, \Delta j, p, C)$ which applies a number of C convolutions with kernel size (n, m) to a 2D input vector I_{ijc} with $\#I_{ijc} = (X, Y, I)$. The stride parameters Δi and Δj allow one to implement dimensional reduction and the parameter p controls if the input data is padded ($p = v$) or unaltered ($p = s$). We provide a thorough mathematical definition of all deep neural network layers used in this work, including the convolutional one, in appendix B1.

Convolution layers are often followed by pooling layers for dimensional reduction. We implement average pooling layers $\text{AvgPool}(n, m, \Delta i, \Delta j, p)$ which average entries of the 2D data vector within a window of size (n, m) , apply a stride defined by Δi and Δj and follow the same padding scheme that was introduced earlier. Maximum pooling layers $\text{MaxPool}(n, m, \Delta i, \Delta j, p)$ work in a similar manner but instead of the average they return the maximum within a given window. Both pooling layers exist also as global versions, indicated by GlobalMaxPool and GlobalAvgPool , where all entries per channel are considered for either the maximum or averaging operation.

Up to this point, we only allowed for layers to be placed strictly sequential. In order to implement a horizontal layout, we connect several layers to the same input and combine their results $I_{ijc_1}, \dots, I_{ijc_n}$ with the help of a concatenation

layer $\text{Concatenate}(I_{ijc_1}, \dots, I_{ijc_n})$. This concept of performing not only one operation at a given depth of the network but several has proven very successful for image classification as e.g. shown in Szegedy et al. (2014), who dubbed such horizontal layers as Inception modules.

The output of a layer can be followed by a non-linear activation function. For convolution and pooling layers we mainly deploy rectangular linear units (ReLU) and we give the full detail about the activation functions used in this work in appendix B2. To avoid the network from overfitting, so-called dropout layers are introduced as a regularisation. In there, a given percentage of the elements of an input vector are chosen at random and are subsequently discarded from the output (Srivastava et al. 2014). Finally, to compensate for fluctuations in the amplitudes of input vectors at different network depth, Ioffe & Szegedy (2015) introduced the concept of batch normalisation which we also use after each convolutional layer. The output of the last layer in the CNN, the feature vector F , is used for classification in a final section of the network which is commonly referred to as top. The concrete architecture of the CNN that we use in this work is provided in section 4.3 and appendix B3.

3.3 Feature-based classification

We now turn our attention to the classification function $\zeta(F; w_m)$. We investigate two different approaches to classification. The first one is a nearest-neighbour-search scheme based on distances in feature space. The other approach, based again on a class of neural networks, uses regression through a training set to find the optimal mapping between features and labels.

3.3.1 Feature space distances

In the following we denote with T all those feature vectors that belong to a sample from the training set and with T^n the subset which belongs only to class n of the training set. We calculate a Fisher discriminant (e.g. Bishop 2006) to find suited classification weights w_m for each individual feature T_i .

$$(w_m)_i = \frac{\sum_{n=1}^N \left(\langle T_i \rangle - \langle T_i^n \rangle \right)^2}{\sum_{n=1}^N (\sigma_{T_i}^n)^2} \frac{N}{N-1} \quad (14)$$

Here N is the total number of classes and $(\sigma_{T_i}^n)^2$ is the variance of the feature i within class n .

Once we found the weights w_m we can define a weighted nearest-neighbour distance (WNN) of any feature vector F to all the classes n in the training set.

$$d_{\text{WNN}}^n = \min_{T \in T^n} \sum_{i=1}^M (w_m)_i (F_i - T_i)^2, \quad (15)$$

where $M = |F|$ is the length of the feature vector. The problem with this WNN distance is the fact that it is based only on a single element in the training set, the one that minimises the sum in equation 15. To remedy this, Orlov et al. (2006) introduced a weighted neighbour distance (WND), which takes into account the distance to all elements in the training set, but largely penalises large distances through the free parameter b

$$d_{\text{WND}}^n = \frac{\sum_{T \in T_c} \left[\sum_{i=1}^M (w_c)_i (F_i - T_i)^2 \right]^b}{|T_c|}. \quad (16)$$

Orlov et al. (2006) found that the results do not strongly depend on b once $b > 2$ and that $b = 5$ is a generally good, numerically stable, choice. The final step in order to make predictions P is to define a similarity using a distance of choice, e.g. WNN or WND, and by normalising appropriately

$$P_n = \left(d_n \sum_{i=1}^N (d_i)^{-1} \right)^{-1}. \quad (17)$$

3.3.2 Fully connected neural networks

A different approach to the classification task is another form of neural network (equation 11). The main layer in such a neural network is a fully connected –sometimes called affine–layer FC(n), which implements a linear mapping between the input vector of length m and the output vector of length n using a matrix of nm free parameters and an additional bias parameter (see appendix B1).

Such layers are again chained together and the last layer produces an output vector of the same length as the number of classes N . As before, in between those layers one may use dropout, activation and normalisation layers. The top of the network is followed by a specific activation function called a softmax (see appendix B2) which provides the desired predictions P_n .

Since the optimal weights w_m are found by a regression, we define a loss function L , which in the case of this classification problem is a categorical cross entropy

$$L(x; w_m) = - \sum_{n=1}^N y_n \log P_n(x; w_m). \quad (18)$$

y are the labels for the elements in the training data x and $P_n(w_m)$ their class predictions given a current set of parameters w_m . In order to minimise the loss, while continuously looping over the training data, we use a specific implementation of stochastic gradient descent called ADAM (Kingma & Ba 2014). The gradients of our model $\frac{d\zeta}{dw_m}$ are thereby calculated via a back-propagation algorithm (Rumelhart et al. 1986). We end this description of our methodology by noting that for a full feature extraction and classification chain $P = \zeta(\Theta(x; w_f); w_m)$, with a CNN as Θ and a neural network as classifier ζ , the classification and feature extraction weights can be optimised at the same time.

3.4 Numerical setup

As mentioned earlier we use the Python package `LensTools`³ (Petri 2016) for the extraction of the standard map descriptors from section 3.2.1. For the computer vision fixed features from section 3.2.2 we slightly adapted the publicly available version of `wnd-charm`⁴. We altered the C++ version of the feature extraction algorithm to accept FITS files (Hanisch et al. 2001) as an input image container with pixel values as double precision floating-point numbers. We then use the feature output files of `wnd-charm` as an input for our own distance-based classification pipeline written in Python. We make these routines publicly available in this repository⁵. All deep learning elements of our analysis stack use the widely used `tensorflow`⁶ framework, which uses NVIDIA’s cuDNN (Chetlur et al. 2014) library to carry out tensor operations on GPUs. We pair a `tensorflow` backend with the high-level deep learning Python interface `keras`⁷ as a frontend. The network training was carried out on two NVIDIA Titan Xp GPUs. All convergence maps and Jupyter⁸ notebooks used to produce the results in this work are either linked to or publicly available in the aforementioned repository. In there, we refer the reader to the ‘reproducible_science’ folder.

4 RESULTS

Section 3 introduced a number of methods to perform mass map characterisation and classification. We now present the results obtained by applying those methods and provide details on their training process with the help of the validation sets. For the most successful method we investigate the dependence of the results on the convergence map source redshift and we end this section with a closer look at the most

³ <https://github.com/apetri/LensTools>

⁴ <https://github.com/wnd-charm/wnd-charm>

⁵ <https://bitbucket.org/jmerten82/mydnn>

⁶ <https://www.tensorflow.org/>

⁷ <https://keras.io/>

⁸ <http://jupyter.org/>

Rank	Name	Index	Weight
1	Power spectrum	11	0.106
2	"	10	0.104
3	"	9	0.092
4	"	12	0.084
5	Peak counts	13	0.083
6	Power spectrum	8	0.078
7	Peak counts	12	0.078
8	Power spectrum	7	0.065
9	Peak counts	5	0.064
10	Skewness	-	0.059
11	Peak counts	14	0.055
12	Power spectrum	6	0.051
13	Percentile	100	0.051
14	Minkowski functional 1	14	0.049
15	Percentile	0	0.049
16	Power spectrum	13	0.046
17	Minkowski functional 2	14	0.045
18	Peak counts	11	0.044
19	Power spectrum	5	0.042
20	Kurtosis	-	0.042

Table 2. The top-ranked classical mass map features according to their Fisher score (equation 14). The meaning of each feature and the explanation of its index can be found in section 3.2.1.

relevant features which are extracted by the different methods. If not stated otherwise, the results in this section are based on training, validation and test set maps at a source redshift $z_s = 1.0$.

4.1 Classification based on feature distance

For the case of the distance-based classifier from section 3.3.1, the training process is just the derivation of the Fisher weights shown in equation 14. We calculate them using the training set and present the 20 top-ranked features for the classical descriptors in table 2 and for the `wnd-charm` features in table 3. For the first case, we see quite a mix of features in the top, with the power spectrum and peak counts being the most important ones. This result is nicely confirmed by the right panel of figure 1, which shows that the bins with $5000 < l < 15000$ of the power spectrum indeed show a clear separation between the more degenerate models. For the `wnd-charm` features however, the ranking is completely dominated by Zernike coefficients on transformations of the image, with a few contributions of Haralick textures. One should keep in mind though that we extract a total of 2919 features, out of which 51 have a weight > 0.1 , 868 have a weight > 0.01 and only 193 features have a vanishing weight. It is the combination of all the non-zero weights which will lead to the distance-based classification later on.

For the 99 standard features we find a total classification success rate of 22%, meaning that out of 14742 samples in the test set, only 3243 were classified correctly. For some specific classes the classification success rate is barely above the success rate for a random guess (11%). The important Λ CDM class for example shows a success rate of 13%. The picture improves marginally when using the 2919 `wnd-charm` features instead. The total classification success over all classes rises mildly to 25%. While especially the three f_6 models still show success rates around or even below 11%, at least some classes, including Λ CDM, are now significantly

Rank	Transform	Name	Index	Weight
1	F	Zernike coefficients	20	0.285
2	F	"	42	0.270
3	F(W)	"	50	0.255
4	F(E)	"	52	0.242
5	F(W)	"	21	0.236
6	F(E)	"	39	0.214
7	F	"	12	0.205
8	F(W)	"	22	0.204
9	F(E)	"	37	0.196
10	F(W)	"	56	0.183
11	F(E)	"	5	0.174
12	F(E)	"	28	0.170
13	W	Haralick textures	5	0.169
14	F	Zernike coefficients	17	0.166
15	F(E)	"	34	0.166
16	F(E)	Haralick textures	0	0.164
17	F(E)	"	14	0.161
18	F(E)	Zernike coefficients	24	0.159
19	F	"	60	0.154
20	-	Edge features	0	0.152

Table 3. The same as table 2 but for the `wnd-charm` features. We refer the reader to appendix A for the definition of each feature and the exact meaning of the feature index and the transform column.

above the 20% level. We do not show more details⁹ on the distance-based classification since it is clear from those results already that this classification method does not qualify for a successful discrimination of our models.

4.2 Classification based on neural network

We now use the same set of fixed features but feed them into a fully-connected neural network for classification. For the case of the 99 standard features we show the very simple topology of the classification network in table 4. The same network is used to classify the 2919 `wnd-charm` features but due to the larger input vector, the number of free parameters is larger, which we indicate by a square bracket notation in the same table. The regression to find the optimal parameters of the main fully-connected layers is based on the training set. In total we train with 110601 feature vectors of shape (1,1,99) or (1,1,2919) and where one iteration over all those elements during the regression is commonly called an epoch. Gradient evaluations and corresponding changes to the network parameters are made after a subset of an epoch, usually called a batch. The batch size in this case was set to 128. After each epoch, we evaluate the current performance of the network with the 22113 (2457 per class) feature vectors in the validation set. Figure 2 shows for both feature sets the evolution of the loss function for the training and validation data as a function of training epoch. For the larger feature vector, the validation loss starts to saturate around epoch 70 while the training loss keeps declining. This indicates that the networks starts to overfit, meaning that it learns training-set specific features which are of no use to characterise the validation set or any data unknown to

⁹ A full success rate analysis is provided in the repository (<https://bitbucket.org/jmerten82/mydnn>) associated with this article.

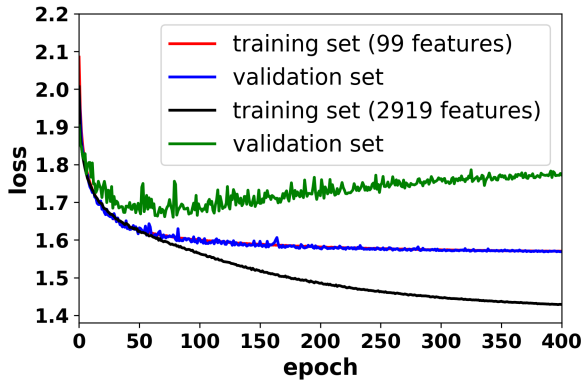


Figure 2. The evolution of the loss as a function of epoch for the training of the neural network. Shown are both cases where either a smaller vector of standard is the input for the network, or a larger set of `wnd-charm` features.

Index	Layer	free parameters	Output shape
1	Input	0	(1,1,99[2919])
2	FC(32)	3200 [93440]	(1,1,32)
3	leakyReLU(0.03)	0	(1,1,32)
4	FC(9)	+297	(1,1,9)
5	Softmax	0	(1,1,9)
Output		=3497 [93737]	9

Table 4. The sequence of layers used in the neural network to classify fixed mass map features. The output shape notation follows the convention introduced in section 3. The description of all layers can be found in sections 3.2.3 and 3.3.2, their formal definition in appendix B1 and B2. The numbers in square brackets refer to the case where the `wnd-charm` feature vector is used instead of the smaller vector of classical features.

the model. This is where we stop the training and save the model parameters which produced the smallest validation loss.

The neural network classification yields significantly better results compared to the classification based on feature-space distances. In the case of the 99 standard features the total classification rate rises to 39% and to 35% in the case of the `wnd-charm` features. Most interestingly, the smaller vector of 99 classical features produces better results than the much larger feature vector provided by `wnd-charm`. Some of the most discriminative features from the computer vision method shown in table 3 are certainly describing the data well and should be used in future analyses; however, once the information from all standard descriptors such as the binned power spectrum, peak counts and Minkowski functionals are combined in an optimal way by a neural network, there is no advantage in using features that are inspired by computer vision only. Table 5 shows the classification success matrix for the standard features, where each row refers to a subset of the test data comprising only maps from that true class labelled by the first column. The first number in each block of four shows how many times the 1638 members of this subset have been sorted into the respective predicted class which is indicated by the label in the very first row. The second number is the percentage of

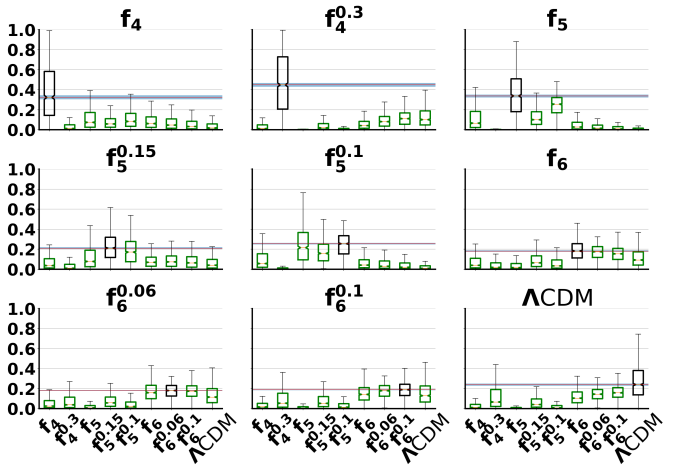


Figure 3. The prediction statistics of the classical feature vector classified by a neural network. Each labelled panel represents all predictions for one true class of the test set. In every panel, each box summarises the statistics of the model predictions indicated by the bottom labels. The median and its bootstrap error for the correct prediction is shown by the red line with error band. For this method only the two f_4 models are clearly distinguished from the other models. Especially the f_5 and f_6 models remain largely degenerate within themselves, but also with Λ CDM.

predictions with respect to the total number of maps in the class. The third and fourth numbers are the mean and its standard error on the prediction probability for all maps in the subset given by the row and for the class predictions indicated by the label of the column. For an optimal classification, only the diagonal of this matrix (those fields typeset in boldface) would show non-zero values.

While table 5 gives a good indication of what to expect from a classification of single maps, only the mean and its standard error on the class predictions give an idea on how well the full ensemble of test set maps is classified. We therefore further evaluate the statistics of the prediction vectors for each true test set class. Figure 3 shows nine panels of box plots, each of which represents the statistics for one such subset. The black box in each panel represents the correct predictions, equivalent to the bold diagonal of table 5. The horizontal line spanning each panel is the median for all the true class predictions and the error band shows the scatter of medians derived from 1000¹⁰ bootstrap samples. The upper and lower end of each box show the 75th and 25th percentiles, respectively, and the whiskers show the outlier cleaned minimum and maximum value of the class predictions. Whenever a box which is not the true label is shown in green, it means that the median and its errors, indicated by the notches of each box, is lower than the one of the correct prediction box and does not overlap with its horizontal error band. If those criteria are not met, the respective box is shown in red.

When looking at the results in table 5 and figure 3, the following observations catch the eye. Although the overall

¹⁰ This number is of course arbitrary but is close to the sample size and we also checked that the bootstrap-derived error does not depend significantly on the number of bootstraps.

	f_4	$f_4^{0.3}$	f_5	$f_5^{0.15}$	$f_5^{0.1}$	f_6	$f_6^{0.06}$	$f_6^{0.1}$	ΛCDM
f_4	958	80	157	103	97	137	26	24	56
	58%	5%	10%	6%	6%	8%	2%	1%	3%
	0.376	0.052	0.122	0.083	0.11	0.087	0.068	0.056	0.046
	± 0.007	± 0.003	± 0.003	± 0.002	± 0.002	± 0.002	± 0.002	± 0.001	± 0.002
$f_4^{0.3}$	70	1135	1	72	10	18	31	116	185
	4%	69%	0%	4%	1%	1%	2%	7%	11%
	0.05	0.468	0.006	0.052	0.018	0.058	0.091	0.12	0.137
	± 0.002	± 0.007	± 0.001	± 0.002	± 0.001	± 0.001	± 0.002	± 0.002	± 0.003
f_5	232	6	857	158	275	84	10	5	11
	14%	0%	52%	10%	17%	5%	1%	0%	1%
	0.129	0.008	0.354	0.129	0.246	0.055	0.036	0.026	0.018
	± 0.004	± 0.001	± 0.005	± 0.003	± 0.002	± 0.002	± 0.001	± 0.001	± 0.001
$f_5^{0.15}$	149	90	173	651	254	120	38	52	111
	9%	5%	11%	40%	16%	7%	2%	3%	7%
	0.082	0.052	0.129	0.229	0.182	0.087	0.086	0.08	0.073
	± 0.003	± 0.002	± 0.002	± 0.002	± 0.002				
$f_5^{0.1}$	223	22	485	333	413	98	18	14	32
	14%	1%	30%	20%	25%	6%	1%	1%	2%
	0.113	0.02	0.249	0.18	0.243	0.067	0.054	0.043	0.031
	± 0.003	± 0.001	± 0.005	± 0.003	± 0.003	± 0.002	± 0.001	± 0.001	± 0.001
f_6	193	103	44	181	65	512	126	171	243
	12%	6%	3%	11%	4%	31%	8%	10%	15%
	0.091	0.061	0.048	0.094	0.065	0.192	0.17	0.155	0.123
	± 0.003	± 0.003	± 0.002	± 0.002	± 0.002	± 0.003	± 0.002	± 0.002	± 0.003
$f_6^{0.06}$	128	194	30	163	39	377	147	257	303
	8%	12%	2%	10%	2%	23%	9%	16%	18%
	0.07	0.095	0.032	0.087	0.05	0.169	0.176	0.176	0.146
	± 0.003	± 0.003	± 0.002	± 0.003					
$f_6^{0.1}$	71	262	18	164	39	279	109	345	351
	4%	16%	1%	10%	2%	17%	7%	21%	21%
	0.049	0.12	0.023	0.086	0.042	0.154	0.176	0.189	0.162
	± 0.002	± 0.004	± 0.001	± 0.002	± 0.003				
ΛCDM	69	265	5	135	9	158	60	166	771
	4%	16%	0%	8%	1%	10%	4%	10%	47%
	0.043	0.14	0.014	0.074	0.028	0.12	0.146	0.164	0.271
	± 0.002	± 0.004	± 0.001	± 0.002	± 0.001	± 0.002	± 0.002	± 0.002	± 0.004

Table 5. The classification success matrix for the neural-network-based classification of the classical features. Each row represents a different subset of the test data indicated by the first column. The first number in each block of four in a column is the number of samples in the subset that was assigned to the predicted class indicated by the column label on the top. The second number is the relative classification success rate for the subset. The third number is the mean of all predictions in the subset and the fourth number is its standard error. The success rates indicate that only the two f_4 models and to a lesser degree f_5 , $f_5^{0.15}$ and ΛCDM are well separated from the other models with correct classification rates of 40% or above and false classification rates for other models of 17% or less. $f_5^{0.1}$ and the two f_6 models with non-vanishing neutrino mass are basically undistinguished from other models and f_6 (success rate 31%) shows still a large degeneracy with ΛCDM (15% misclassification rate).

classification success rate is only 39%, none of the classes is classified incorrectly as an ensemble. In the case of the two f_4 models we see a clear separation between the correct predictions from the other classes. This is confirmed by the classification matrix, which shows no substantial overlap ($> 11\%$) with any other model. This however changes for the three f_5 and the three f_6 models. Although the median for the correct predictions is the highest for all of the models¹¹, the degeneracies within the same model of gravity are strong in those cases as one can see from the basically equal

heights of the centres of the boxes in figure 3 and from the classification matrix, which lists a large number of misclassifications up to 30% in the case of $f_5^{0.1}$ misclassified as f_5 . A lot more severe is the case of the three f_6 models. For them we find substantial overlap of up to 21% with ΛCDM . Even the predictions for ΛCDM itself are not completely separate from the three f_6 models and $f_4^{0.3}$ with an overlap of up to 16%.

¹¹ The mean is not in the case of $f_5^{0.1}$

Layer		free parameters	Output shape
1	Input	0	(256,256,1)
2	Conv(3,3,2,2,v,32)*	288	(127,127,32)
3	lReLU(0.03)	0	(127,127,32)
4	Conv(3,3,1,1,v,32)*	+9216	(125,125,32)
5	lReLU(0.03)	0	(125,125,32)
6	Conv(3,3,1,1,s,64)*	+9216	(125,125,32)
7	StemInception* (Fig. B1)	+555008	(29,29,384)
8	InceptionA* (Fig. B2)	+316416	(29,29,384)
9	ReductionA* (Fig. B3)	+2304000	(14,14,1024)
10	InceptionB* (Fig. B4)	+2931712	(14,14,1024)
11	ReductionB* (Fig. B5)	+2744320	(6,6,1536)
12	InceptionC* (Fig. B6)	+4546560	(6,6,1536)
13	GlobalAvgPool	0	(1,1,1536)
14	Dropout(0.33)	0	(1,1,1536)
15	FC(9)	+13833	(1,1,9)
16	Softmax	0	(1,1,9)
17	Ouput	=13469865	9

Table 6. The sequential structure of the CNN used in this work. All layers marked by * are batch normalised. More complicated Inception layers are shown in the respective figure.

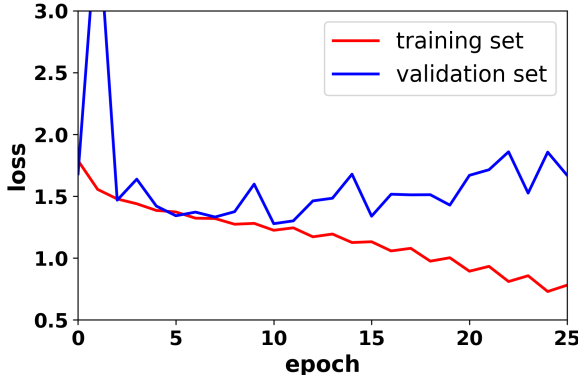


Figure 4. The evolution of the loss as a function of epoch for the training of the CNN.

4.3 Convolutional neural network

The convolutional neural network (CNN) extracts the characterising features directly from the pixel data of the training mass maps. We have experimented with a number of architectures, including classic topologies which implement a large number of 3×3 convolutions inspired by VGG-net (Simonyan & Zisserman 2014), as well as architectures presented in Ravanbakhsh et al. (2017) and Gupta et al. (2018). The model that worked best for our purposes is almost exclusively based on the Inception layers first presented in Szegedy et al. (2014). Here we adopt one of its latest iterations, version 4 introduced in Szegedy et al. (2016). The global linear structure of our CNN is shown in table 6 and we describe in detail the different elements of this network and their purpose in appendix B3. We visualise the evolution of the network’s loss during training in figure 4.

The total classification success rate of the CNN is 52% and its classification success matrix is shown in table 7. Compared to the fixed feature results in table 5 we find much larger true prediction values for many models. Exceptions

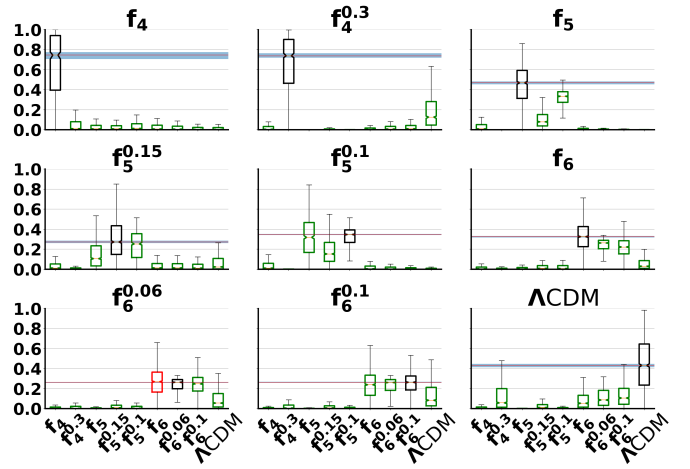


Figure 5. Prediction statistics for the CNN at source redshift $z_s = 1$. The structure of the figure is the same as in figure 3. The CNN discriminates more clearly between the models and both f_4 models, f_5 and Λ CDM are now clearly distinguished. Problems remain for the different neutrino mass realisations within f_6 and f_5 gravity. $f_6^{0.06}$ is incorrectly classified as $f_6^{0.1}$.

are $f_5^{0.1}$ and $f_6^{0.06}$. Figure 5 shows the statistics of the predictions for all classes in the test set and reveals that the $f_6^{0.06}$ and $f_6^{0.1}$ models, even as an ensemble, cannot be classified correctly by the CNN since the error bars on the medians of the predictions in their samples overlap with other f_6 models. However, the degeneracy with Λ CDM is now broken for all models and the CNN robustly discriminates most of the nine models from each other.

4.4 Dependence on redshift

A source redshift of $z_s = 1$ is realistic for future space -and ground-based surveys but it is certainly optimistic for current ground-based surveys. On the other hand, it also does not test the full potential of our classification methods since one would expect a better classification accuracy for larger source redshifts. We therefore repeat training and classification for one lower ($z_s = 0.5$) and one higher ($z_s = 2$) source redshift. For simplicity we restrict this analysis to the CNN which delivered the best results.

For a source redshift $z_s = 0.5$ the overall accuracy drops significantly from 52% to 44%. When comparing the prediction statistics of the full set at this redshift in figure 6 with the reference at $z_s = 1$ in figure 5, one can see that the decrease in the overall accuracy mainly stems from a weaker separation of the two f_4 models, f_5 and Λ CDM. The known issue of degeneracies between the three neutrino masses for f_5 and f_6 are already present and more prominent. The issue of model misclassification for f_6 gravity gets worse with now two misclassifications. The improvements when going from $z_s = 1$ to $z_s = 2$ are highlighted by figure 7. For $z_s = 2$ the network’s ability to distinguish between the base models increases and the overall classification accuracy is now 59%. The discrimination accuracy for massive neutrinos within each gravity model increases for the f_5 models and only the two f_6 models with massive neutrinos show significant overlap. Those models are also the only ones that show residual,

	f_4	$f_4^{0.3}$	f_5	$f_5^{0.15}$	$f_5^{0.1}$	f_6	$f_6^{0.06}$	$f_6^{0.1}$	ΛCDM
f_4	1307	116	36	21	31	88	12	5	22
	80%	7%	2%	1%	2%	5%	1%	0%	1%
	0.646	0.085	0.045	0.035	0.05	0.049	0.036	0.025	0.028
	± 0.008	± 0.004	± 0.002	± 0.001	± 0.002				
$f_4^{0.3}$	51	1298	0	11	0	7	8	27	236
	3%	79%	0%	1%	0%	0%	0%	2%	14%
	0.046	0.658	0.001	0.014	0.004	0.02	0.031	0.037	0.19
	± 0.003	± 0.007	± 0.0	± 0.001	± 0.0	± 0.001	± 0.001	± 0.002	± 0.005
f_5	105	1	1065	90	320	48	2	1	6
	6%	0%	65%	5%	20%	3%	0%	0%	0%
	0.064	0.002	0.444	0.114	0.316	0.028	0.016	0.011	0.006
	± 0.003	± 0.0	± 0.005	± 0.003	± 0.002	± 0.002	± 0.001	± 0.001	± 0.001
$f_5^{0.15}$	103	37	161	721	347	78	14	31	146
	6%	2%	10%	44%	21%	5%	1%	2%	9%
	0.059	0.031	0.153	0.3	0.235	0.048	0.044	0.041	0.088
	± 0.003	± 0.002	± 0.004	± 0.005	± 0.003	± 0.002	± 0.002	± 0.002	± 0.004
$f_5^{0.1}$	122	5	624	271	514	70	5	7	20
	7%	0%	38%	17%	31%	4%	0%	0%	1%
	0.071	0.007	0.323	0.187	0.315	0.036	0.025	0.019	0.018
	± 0.004	± 0.001	± 0.005	± 0.004	± 0.003	± 0.002	± 0.001	± 0.001	± 0.001
f_6	51	27	11	42	44	968	74	307	114
	3%	2%	1%	3%	3%	59%	5%	19%	7%
	0.035	0.022	0.023	0.034	0.036	0.326	0.235	0.218	0.072
	± 0.002	± 0.002	± 0.001	± 0.002	± 0.002	± 0.004	± 0.002	± 0.002	± 0.003
$f_6^{0.06}$	36	46	11	40	35	713	95	458	204
	2%	3%	1%	2%	2%	44%	6%	28%	12%
	0.026	0.036	0.017	0.034	0.029	0.271	0.235	0.24	0.112
	± 0.002	± 0.002	± 0.001	± 0.002	± 0.002	± 0.003	± 0.002	± 0.002	± 0.004
$f_6^{0.1}$	20	79	5	35	17	558	64	565	295
	1%	5%	0%	2%	1%	34%	4%	34%	18%
	0.018	0.05	0.01	0.03	0.02	0.24	0.23	0.253	0.149
	± 0.001	± 0.003	± 0.001	± 0.001	± 0.001	± 0.003	± 0.002	± 0.002	± 0.004
ΛCDM	41	179	0	43	3	99	43	144	1086
	3%	11%	0%	3%	0%	6%	3%	9%	66%
	0.027	0.141	0.005	0.04	0.014	0.087	0.111	0.129	0.445
	± 0.002	± 0.005	± 0.0	± 0.002	± 0.001	± 0.002	± 0.002	± 0.002	± 0.006

Table 7. The classification success matrix for the CNN. The general structure of the table is the same as in table 5. We see successful classifications of the two f_4 models, f_5 , f_6 and ΛCDM . However, large degeneracies remain within the neutrino mass variants of f_5 and f_6 gravity, respectively. In some cases, the wrong predictions can outnumber the correct ones as is the case for $f_5^{0.1}$ and $f_6^{0.06}$.

but insignificant overlap with ΛCDM . Given the fact that the ensemble of $f_6^{0.1}$ maps also gets misidentified as $f_6^{0.06}$, it is clear that the discrimination within the f_6 models remains an issue even at a larger source redshift.

As a last analysis using the CNN we perform a tomographic classification. For each line-of-sight realisation we are not using a single mass map at a specific source redshift but we feed data vectors of shape $\#x = (256, 256, 4)$ into the CNN where the four channels refer to $z_s = 0.5$, $z_s = 1$, $z_s = 1.5$ and $z_s = 2$, respectively. The classification success matrix for this analysis is shown in table 8 and figure 8 shows the familiar box-plot representation of the prediction-vector statistics. The overall classification success rate rises to 76% and all models besides $f_6^{0.06}$ and $f_6^{0.1}$ now show correct classification rates of 74% or clearly above. The probability of correctly classifying a single map in those two models are only 38% or 50%, respectively, however, a look at figure 8

reveals that they are correctly classified as an ensemble and at high significance. Finally, it is worth noting that none of the models shows any degeneracy with ΛCDM which is larger than 4% according to table 8.

4.5 Remarks on extracted features

After presenting the raw classification results for different methods, we now briefly investigate what insight can be gathered into the actual meaning and importance of specific features that drive the classification success of different methods. To do so, we take a closer look at the training process. The first important observation is strikingly highlighted in table 3, which shows that almost all of the most discriminating `wnd-charm` features are Zernike coefficients derived from the Fourier transform of the raw image or from the Fourier transform of the edge -or wavelet-processed im-

	f_4	$f_4^{0.3}$	f_5	$f_5^{0.15}$	$f_5^{0.1}$	f_6	$f_6^{0.06}$	$f_6^{0.1}$	ΛCDM
f_4	1618 99% 0.985 ± 0.002	0 0% 0.0 ± 0.0	7 0% 0.007 ± 0.002	0 0% 0.0 ± 0.0	10 1% 0.006 ± 0.001	3 0% 0.002 ± 0.001	0 0% 0.0 ± 0.0	0 0% 0.0 ± 0.0	0 0% 0.0 ± 0.0
$f_4^{0.3}$	0 0% 0.0 ± 0.0	1501 92% 0.91 ± 0.006	0 0% 0.0 ± 0.0	1 0% 0.001 ± 0.0	0 0% 0.0 ± 0.0	0 0% 0.001 ± 0.0	1 1% 0.002 ± 0.001	20 7% 0.015 ± 0.002	115 7% 0.072 ± 0.005
f_5	3 0% 0.001 ± 0.001	0 0% 0.0 ± 0.0	1257 77% 0.748 ± 0.008	2 0% 0.002 ± 0.001	375 23% 0.247 ± 0.008	1 0% 0.001 ± 0.001	0 0% 0.0 ± 0.0	0 0% 0.0 ± 0.0	0 0% 0.0 ± 0.0
$f_5^{0.15}$	0 0% 0.0 ± 0.0	0 0% 0.0 ± 0.0	1 0% 0.001 ± 0.001	1470 90% 0.873 ± 0.007	96 6% 0.071 ± 0.005	22 1% 0.015 ± 0.002	7 0% 0.009 ± 0.001	2 0% 0.004 ± 0.001	40 2% 0.027 ± 0.003
$f_5^{0.1}$	0 0% 0.001 ± 0.0	0 0% 0.104 ± 0.005	130 8% 0.148 ± 0.007	207 13% 0.74 ± 0.007	1289 79% 0.74 ± 0.008	12 1% 0.008 ± 0.002	0 0% 0.0 ± 0.0	0 0% 0.0 ± 0.0	0 0% 0.0 ± 0.0
f_6	0 0% 0.0 ± 0.0	0 0% 0.0 ± 0.0	0 0% 0.01 ± 0.002	15 1% 0.01 ± 0.002	1 0% 0.001 ± 0.0	1206 74% 0.676 ± 0.008	275 17% 0.194 ± 0.005	30 2% 0.046 ± 0.003	111 7% 0.073 ± 0.005
$f_6^{0.06}$	0 0% 0.0 ± 0.0	0 0% 0.0 ± 0.0	0 0% 0.005 ± 0.001	7 0% 0.0 ± 0.0	0 0% 0.0 ± 0.0	363 22% 0.226 ± 0.007	627 38% 0.344 ± 0.005	319 19% 0.233 ± 0.006	322 20% 0.191 ± 0.007
$f_6^{0.1}$	0 0% 0.0 ± 0.0	3 0% 0.002 ± 0.001	0 0% 0.0 ± 0.0	3 0% 0.002 ± 0.001	0 0% 0.0 ± 0.0	77 5% 0.064 ± 0.004	385 24% 0.272 ± 0.005	827 50% 0.455 ± 0.008	343 21% 0.204 ± 0.008
ΛCDM	0 0% 0.0 ± 0.0	1 0% 0.001 ± 0.001	0 0% 0.0 ± 0.0	6 0% 0.006 ± 0.001	0 0% 0.0 ± 0.0	57 3% 0.039 ± 0.003	69 4% 0.059 ± 0.003	37 2% 0.044 ± 0.003	1468 90% 0.85 ± 0.007

Table 8. The classification success matrix for the tomographic analysis using the CNN. The general structure of the table is the same as in table 5. We see good classification rates above 79% and typically above 90% for all models but the f_6 -family. Also f_6 with vanishing neutrino mass is correctly classified 74% of the time. The remaining degeneracies are limited to $f_6^{0.06}$ and $f_6^{0.1}$ with 38% and 50% classification accuracy, respectively, but given the error bars on the prediction mean the degeneracy is not significant for the ensemble of mass maps in the test set.

age. This is interesting since Zernike polynomials were originally introduced to describe the effects of certain optical elements such as lenses or reflecting surfaces in optical imaging (Zernike 1934). This suggests that a decomposition of mass maps into a function set that has a well-defined physical meaning does indeed lead to a good general representation of our data. In addition, all those features are derived from transformations of the raw mass map which shows the power of filtering the input data as e.g. shown by Peel et al. (2018). The ranking of the standard features shown in table 2 is less dominated by a single class, although the power spectrum and peak counts seem most relevant. The good results with a neural network as classifier shows that the optimal combination of such classical features leads to a good classification even without the need for additional descriptors.

CNNs often deliver superior results compared to other methods for certain tasks, but it is often believed that they are harder to understand and interpret. We are attempting to dissolve this belief by applying visualisation techniques for the different filters linked together in a deep neural network (Girshick et al. 2013; Zeiler & Fergus 2013; Szegedy et al. 2013; Springenberg et al. 2014) and in order to reveal the inner workings of the complex model. We follow the approach of Simonyan et al. (2013) to extract our filter responses¹². Starting from an image of random numbers

12

Also see https://github.com/keras-team/keras/blob/master/examples/conv_filter_visualization.py

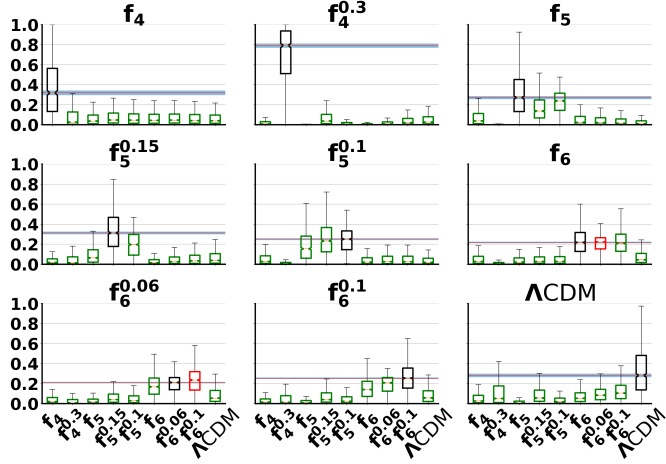


Figure 6. Prediction statistics for the CNN and a source redshift of $z_s = 0.5$. Compared to figure 5, the separation between the models becomes washed out. Two misclassifications occur: f_6 is incorrectly classified as $f_6^{0.06}$ and $f_6^{0.06}$ is misclassified as $f_6^{0.1}$. Also, the $f_5^{0.1}$ samples cannot be distinguished as an ensemble from the $f_5^{0.15}$ ones since their prediction medians overlap within the error bars.

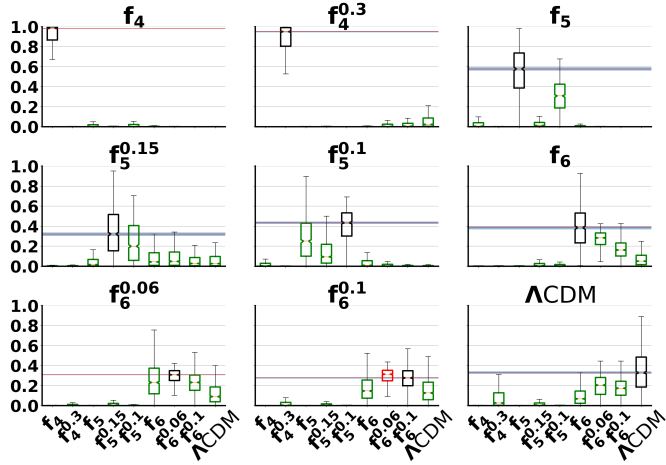


Figure 7. Prediction statistics for the CNN and at a source redshift of $z_s = 2$. Only the $f_6^{0.1}$ model remains degenerate given the error bar on the median of its sample predictions. In fact it is misclassified as $f_6^{0.06}$ by the CNN.

with the same shape as our mass maps, we retrieve the output of every convolutional layer in the network and perform a gradient ascent in order maximise the response of those layers. While this is of course not a unique solution, the result of the final iteration of the ascent represents an example which triggered a strong response at a particular depth in the network. In figure 9 we show a few examples. The top row shows the four channels which had the strongest loss compared to the initial random image in CNN layer one. That is the 3×3 convolution marked with index 2 in table 6. The second row shows the top four channel responses of the 3×3 convolution with stride two just above the input layer in figure B1. The row marked with InceptionA shows the

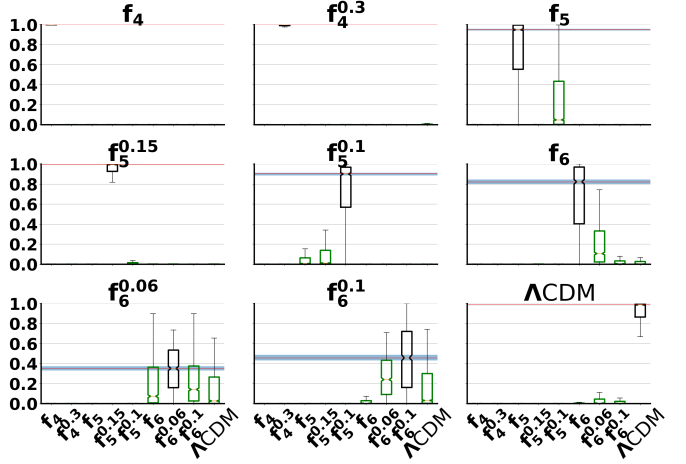


Figure 8. Predictions statistics on the tomographic analysis with the CNN. For many classes the classification is so good, that the prediction samples cluster around the optimal value of 1. All models are correctly classified and within the error bars of the prediction medians, no model remains observationally degenerate. Only small similarities remain between the three f_6 models of varying neutrino mass.

most responsive channels among all four convolutions just below the concatenation layer in figure B1 and equivalently for the figure rows marked InceptionB and C. As is typical for CNNs (Zeiler & Fergus 2013), the very first level extracts very regular horizontal and vertical stripe patterns from the image. The stripes turn into a grid pattern deeper into the network and once arriving at the end of the InceptionA layer we can identify patterns of peaks and troughs which are either grouped regularly or along larger structures. It is not surprising that the earlier layers of the network, up to InceptionA, perform a global filtering of the map that highlights structure as long as the image still consists of a relatively large number of pixels. It is just from the finer InceptionB layers on that more specific structures, like objects that look like individual clusters or voids are picked up. It is such detailed analyses of the inner structure of trained CNNs that will lead to a deeper understanding why those networks work so well. This can potentially lead to the development of more specific algorithms at lower numerical cost but with similar or better classification performance.

5 CONCLUSIONS

We studied the ability of different kinds of machine learning techniques to discriminate between highly degenerate cosmological models, which combine the effects of modified gravity and massive neutrinos on structure formation. For this purpose we used a subset of the DUSTGRAIN-*pathfinder* simulation suite which consists of Λ CDM and eight $f(R)$ models of gravity in the range of $-1 \times 10^{-4} \leq f_{R0} \leq -1 \times 10^{-6}$. The neutrino masses in the simulations span $0 \text{ eV} \leq m_\nu \leq 0.3 \text{ eV}$. Lensing convergence maps produced from these simulations provided the input for the different classification methods.

In order to characterise the mass maps we used three

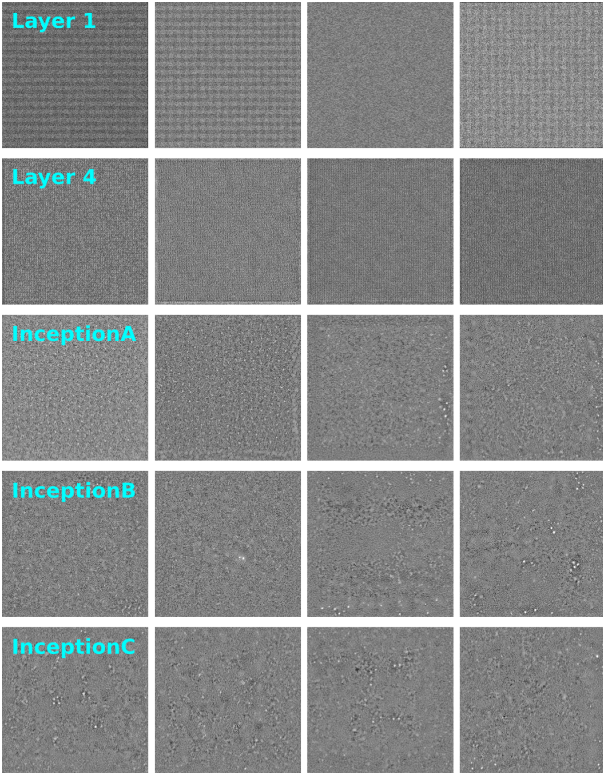


Figure 9. Visualisations of the convolutional filters applied by the CNN at different depths of the network.

different approaches to feature extraction. Commonly used statistics in astrophysics such as, and among others, the power spectrum, peak counts and Minkowski functionals were combined into a single feature vector. In order to probe features which are more common to the field of computer vision and digital image processing, we used the publicly available `wnd-charm` algorithm which produces a large feature vector that combines a variety of common and more exotic descriptors and statistics. As the most flexible method of feature extraction we used a convolutional neural network (CNN). For classification we tested a nearest-neighbour method in feature space and a fully-connected neural network.

We provide an overview of the classification results from section 4 in table 9 and our results can be summarised as follows:

(i) Nearest-neighbour classifiers based on distances in feature space are not delivering robust results. No matter if a small classical feature vector is used or a longer version based on computer vision, the total classification accuracy stays below 25%. Eight, out of the nine tested models, remain observationally degenerate¹³.

(ii) With the same classical or computer vision feature vectors, a neural network delivers a much more robust classification than the nearest-neighbour method. The total suc-

¹³ We declare a model as degenerate if the median and its error for the predictions of a true test set class overlaps with the median and its error of the predictions for any other class.

cess rate for the classical feature vector is 39% and the number of degenerate models reduces to three.

(iii) The longer feature vector containing 2919 features inspired by computer vision delivers a slightly worse classification of our models than the shorter vector with 99 classical descriptors. The total classification success rate is 3% lower and the method produces one additional degenerate model. Some of the computer vision feature may very well be useful, but currently we see no advantage of using features inspired by digital image processing compared to features well-established in cosmology.

(iv) A CNN delivers the best classification results with 52% correct classifications at source redshift $z_s = 1.0$. The number of degenerate models reduces to two, both of which are part of the same f_6 model of gravity.

(v) Classification success is clearly a function of mass map source redshift. While going from $z_s = 1$ to $z_s = 0.5$ the success rate of the CNN decreases by 8% and the number of degenerate models increases by one. When going from $z_s = 1$ to $z_s = 2$ the accuracy increases by 7% and the number of degenerate models reduces by one. This increase of success rate with increasing redshift is not surprising since more information relevant to structure formation can be picked up along a deeper line-of-sight.

(vi) When using a CNN in a tomographic analysis of four different mass map source redshifts along the same line-of-sight all observational degeneracies are fully broken. The total classification success rate increases to 76%.

A number of improvements to our methodology come to mind and we reserve them for future work. Firstly, the flexible features derived by a CNN can be combined with fixed features that are known to contribute to a successful classification of degenerate models. Secondly, instead of working on the raw image data, a clever transformation can be applied to the input data to enhance features that allow for the desired discrimination. We attempt such an approach in the context of machine learning in Peel et al. (2018b, PRL submitted). In fact, the CNN used in this work applies such transformations as we discussed in section 4.5. A careful analysis of the filtering process of a CNN at the early levels of its filter chain can provide useful insight into the most powerful image transformation for a given classification task. Furthermore, the careful analysis of the filters at a much deeper level of the network might actually lead to more insights on structure formation in different models, since it is at this deeper level where individual structure is characterised and isolated by the algorithm.

Much work is left to be done before this machine learning approach to the classification of mass maps in different cosmological models can be applied to real data. In this work we limited ourselves to optimal noise-free maps in order to see how different methodologies compare under optimal conditions. The influence of pixel shot-noise, observational systematics and practical issues like masking and image artefacts needs to be studied in detail. Furthermore, since the currently most successful methods use a supervised training process with labelled data based on numerical simulations, it needs to be carefully investigated how closely those simulated maps resemble a real observation. Without this important sanity check, even the best machine learning technique is useless since it learns the wrong data.

Θ	ζ	z_s	total accuracy	degenerate classes	Λ CDM performance	Reference
classic	nearest neighbour	1.0	22%	8	14%/15% ($f_4^{0.3}$)	repository
wnd-charm	nearest neighbour	1.0	25%	7	24%/24% ($f_4^{0.3}$)	repository
classic	neural network	1.0	39%	3	47%/16% ($f_4^{0.3}$)	Tab. 5, Fig. 3
wnd-charm	neural network	1.0	36%	4	42%/24% ($f_4^{0.3}$)	repository
CNN	neural network	0.5	44%	3	52%/15% ($f_4^{0.3}$)	Fig. 6
CNN	neural network	1.0	52%	2	66%/11% ($f_4^{0.3}$)	Tab. 7, Fig. 5
CNN	neural network	2.0	59%	1	53%/12% ($f_4^{0.3}$)	Fig. 7
CNN	neural network	0.5, 1.0, 1.5, 2.0	76%	0	90%/4% ($f_6^{0.06}$)	Tab. 8, Fig. 8

Table 9. A summary of the performance of the different methods used in this analysis. Θ indicates the feature extraction function as described in section 3.2. ζ is the classification function introduced in section 3.3 and z_s is the convergence map source redshift. Degenerate classes is the number of all models for which the median and its error for the predictions of the true test set class overlaps with the median and its error of the predictions for any other class. The table also lists the performance for the particularly important Λ CDM class and shows the classification accuracy of each method for this model as well as the largest misclassification rate and the associated model. A reference to the detailed results of each models is given in the last column, where the reference ‘repository’ points to the online repository mentioned in section 3.4.

ACKNOWLEDGEMENTS

We would like to thank Ofer Springer for useful discussions about deep learning. JM has received funding from the European Union’s Horizon 2020 research and Innovation programme under the Marie Skłodowska-Curie grant agreement No 664931. AP acknowledges support from an Enhanced Eurotalents Fellowship, a Marie Skłodowska-Curie Actions Programme co-funded by the European Commission and Commissariat à l’énergie atomique et aux énergies alternatives (CEA). CG and MB acknowledge support from the Italian Ministry for Education, University and Research (MIUR) through the SIR individual grant SIMCODE (project number RBSI14P4IH). CG and MM acknowledge support from the Italian Ministry of Foreign Affairs and International Cooperation, Directorate General for Country Promotion (Project “Crack the lens”). We also acknowledge the support from the grant MIUR PRIN 2015 “Cosmology and Fundamental Physics: illuminating the Dark Universe with Euclid”; and the financial contribution from the agreement ASI n.I/023/12/0 “Attività relative alla fase B2/C per la missione Euclid”. The DUSTGRAIN-*pathfinder* simulations analyzed in this work have been performed on the Marconi supercomputing machine at Cineca thanks to the PRACE project SIMCODE1 (grant nr. 2016153604) and on the computing facilities of the Computational Center for Particle and Astrophysics (C2PAP) and of the Leibniz Supercomputer Center (LRZ) under the project ID pr94ji. We gratefully acknowledge the support of NVIDIA Corporation with the donation of the two Titan Xp GPUs used for this research.

REFERENCES

- ATLAS Collaboration 2013, preprint, ([arXiv:1309.4017](#))
- Aartsen M. G., et al., 2013, *Physical Review Letters*, **110**, 131302
- Abbott T. M. C., et al., 2018, *Phys. Rev. D*, **98**, 043526
- Abraham R. G., van den Bergh S., Nair P., 2003, *ApJ*, **588**, 218
- Ackermann M., et al., 2017, *ApJ*, **840**, 43
- Alam S., et al., 2017, *MNRAS*, **470**, 2617
- Albert A., et al., 2017, *ApJ*, **834**, 110
- Amendola L., et al., 2018, *Living Reviews in Relativity*, **21**, 2
- Arnold C., Puchwein E., Springel V., 2014, *MNRAS*, **440**, 833
- Arnold C., Puchwein E., Springel V., 2015, *Mon. Not. Roy. Astron. Soc.*, **448**, 2275
- Arnold C., Springel V., Puchwein E., 2016, *MNRAS*, **462**, 1530
- Arnold C., Fosalba P., Springel V., Puchwein E., Blot L., 2018, ArXiv e-prints 1805.09824,
- Baldi M., Villaescusa-Navarro F., 2018, *Mon. Not. Roy. Astron. Soc.*, **473**, 3226
- Baldi M., Villaescusa-Navarro F., Viel M., Puchwein E., Springel V., Moscardini L., 2014, *Mon. Not. Roy. Astron. Soc.*, **440**, 75
- Barreira A., Llinares C., Bose S., Li B., 2016, *J. Cosmology Astropart. Phys.*, **5**, 001
- Bartelmann M., Schneider P., 2001, *Phys. Rep.*, **340**, 291
- Benitez N., et al., 2014, ArXiv e-prints 1403.5237,
- Bennett C., et al., 2013, *Astrophys.J.Suppl.*, **208**, 20
- Bernabei R., et al., 2018, *Journal Nucl. Phys. and Atomic Energy*, **19**, 307
- Bishop C. M., 2006, *Pattern Recognition and Machine Learning (Information Science and Statistics)*. Springer-Verlag New York, Inc., Secaucus, NJ, USA
- Buchdahl H. A., 1970, *MNRAS*, **150**, 1
- CMS Collaboration 2016, preprint, ([arXiv:1603.08914](#))
- Castro T., Quartin M., Giocoli C., Borgani S., Dolag K., 2018, *MNRAS*, **478**, 1305
- Chetlur S., Woolley C., Vandermersch P., Cohen J., Tran J., Catanzaro B., Shelhamer E., 2014, CoRR, abs/1410.0759
- Chollet F., 2017, *Deep Learning with Python*, 1st edn. Manning Publications Co., Greenwich, CT, USA
- Dietrich J. P., Hartlap J., 2010, *MNRAS*, **402**, 1049
- Fogel I., Sagi D., 1989, *Biological Cybernetics*, **61**, 103
- Friedrich O., et al., 2018, *Phys. Rev. D*, **98**, 023508
- Fu L., et al., 2008, *Astron. Astrophys.*, **479**, 9
- Giocoli C., Meneghetti M., Metcalf R. B., Ettori S., Moscardini L., 2014, *MNRAS*, **440**, 1899
- Giocoli C., et al., 2016, *MNRAS*, **461**, 209
- Giocoli C., et al., 2017, *MNRAS*, **470**, 3574
- Giocoli C., Baldi M., Moscardini L., 2018a, ArXiv e-prints: 1806.04681,
- Giocoli C., Moscardini L., Baldi M., Meneghetti M., Metcalf R. B., 2018b, *MNRAS*,
- Girshick R., Donahue J., Darrell T., Malik J., 2013, preprint, ([arXiv:1311.2524](#))
- Goodfellow I., Bengio Y., Courville A., 2016, *Deep Learning*. The MIT Press
- Graves A., 2013, CoRR, abs/1308.0850
- Gruen D., et al., 2018, *Phys. Rev. D*, **98**, 023507
- Gupta A., Matilla J. M. Z., Hsu D., Haiman Z., 2018, *Phys. Rev. D*, **97**, 103515
- Hagstotz S., Costanzi M., Baldi M., Weller J., 2018, ArXiv e-prints 1806.07400,
- Hanisch R. J., Farris A., Greisen E. W., Pence W. D., Schlesinger

- B. M., Teuben P. J., Thompson R. W., Warnock III A., 2001, *A&A*, **376**, 359
- Haralick R. M., Shanmugam K., Dinstein I., 1973, *IEEE Transactions on Systems, Man, and Cybernetics*, SMC-3, 610
- He J.-h., 2013, arXiv:1307.4876,
- He K., Zhang X., Ren S., Sun J., 2015, preprint, ([arXiv:1512.03385](https://arxiv.org/abs/1512.03385))
- Herbel J., Kacprzak T., Amara A., Refregier A., Lucchi A., 2018, *J. Cosmology Astropart. Phys.*, **7**, 054
- Heymans C., et al., 2012, *MNRAS*, **427**, 146
- Hikage C., et al., 2018, preprint, ([arXiv:1809.09148](https://arxiv.org/abs/1809.09148))
- Hilbert S., White S. D. M., Hartlap J., Schneider P., 2008, *MNRAS*, **386**, 1845
- Hilbert S., Hartlap J., White S. D. M., Schneider P., 2009, *A&A*, **499**, 31
- Hildebrandt H., et al., 2017, *MNRAS*, **465**, 1454
- Hu W., Sawicki I., 2007, *Phys. Rev.*, D76, 064004
- Ioffe S., Szegedy C., 2015, CoRR, abs/1502.03167
- Ivezic Z., et al., 2008, arXiv:0805.2366
- Johnson M., et al., 2016, CoRR, abs/1611.04558
- Joudaki S., et al., 2017, *MNRAS*, **465**, 2033
- Kingma D. P., Ba J., 2014, CoRR, abs/1412.6980
- Kratochvil J. M., Haiman Z., May M., 2010, *Phys. Rev. D*, **81**, 043519
- Kratochvil J. M., Lim E. A., Wang S., Haiman Z., May M., Huffenberger K., 2012, *Phys. Rev. D*, **85**, 103513
- Krizhevsky A., Sutskever I., Hinton G. E., 2012, in Pereira F., Burges C. J. C., Bottou L., Weinberger K. Q., eds., *Advances in Neural Information Processing Systems 25*. Curran Associates, Inc., pp 1097–1105
- Laureijs R., et al., 2011, eprint arXiv: 1110.3193,
- LeCun Y., Bengio Y., Hinton G., 2015, *Nature*, **521**, 436
- Lin C.-A., Kilbinger M., 2018, *A&A*, **614**, A36
- Lin T., Goyal P., Girshick R. B., He K., Dollár P., 2017, CoRR, abs/1708.02002
- Lucie-Smith L., Peiris H. V., Pontzen A., Lochner M., 2018, *MNRAS*, **479**, 3405
- Martinet N., et al., 2018, *MNRAS*, **474**, 712
- Motohashi H., Starobinsky A. A., Yokoyama J., 2013, *Phys.Rev.Lett.*, **110**, 121302
- Naik A. P., Puchwein E., Davis A.-C., Arnold C., 2018, ArXiv e-prints 1805.12221,
- Ntampaka M., et al., 2018, preprint, ([arXiv:1810.07703](https://arxiv.org/abs/1810.07703))
- Orlov N., Johnston J., Macura T., Wolkow C., Goldberg I., 2006, in 3rd IEEE International Symposium on Biomedical Imaging: Nano to Macro, 2006.. pp 1152–1155, doi:10.1109/ISBI.2006.1625127
- Orlov N., Shamir L., Macura T., Johnston J., Eckley D. M., Goldberg I. G., 2008, Pattern recognition letters, **29**, 1684
- Otsu N., 1979, *IEEE Transactions on Systems, Man, and Cybernetics*, **9**, 62
- Parkinson D., et al., 2012, *Phys. Rev. D*, **86**, 103518
- Peel A., Lin C.-A., Lanusse F., Leonard A., Starck J.-L., Kilbinger M., 2017, *A&A*, **599**, A79
- Peel A., Pettorino V., Giocoli C., Starck J.-L., Baldi M., 2018, preprint, ([arXiv:1805.05146](https://arxiv.org/abs/1805.05146))
- Perlmutter S., et al., 1999, *Astrophys. J.*, **517**, 565
- Petri A., 2016, *Astronomy and Computing*, **17**, 73
- Petri A., Liu J., Haiman Z., May M., Hui L., Kratochvil J. M., 2015, *Phys. Rev. D*, **91**, 103511
- Petri A., Haiman Z., May M., 2017, *Phys. Rev. D*, **95**, 123503
- Pezzotta A., et al., 2017, *A&A*, **604**, A33
- Planck Collaboration et al., 2016a, *A&A*, **594**, A13
- Planck Collaboration et al., 2016b, *A&A*, **594**, A24
- Planck Collaboration et al., 2018, ArXiv e-prints 1807.06209,
- Prewitt J., 1970, Picture Processing and Psychopictorics. New York: Academic Press
- Puchwein E., Baldi M., Springel V., 2013, *MNRAS*, **436**, 348
- Radon J., 1917, in Berichte über die Verhandlungen der Königlich-Sächsischen Akademie der Wissenschaften zu Leipzig. Teubner, pp 262–277, doi:doi:10.1109/TMI.1986.4307775, <https://dx.doi.org/10.1109/2FTMI.1986.4307775>
- Ravanbakhsh S., Oliva J., Fromenteau S., Price L. C., Ho S., Schneider J., Poczos B., 2017, preprint, ([arXiv:1711.02033](https://arxiv.org/abs/1711.02033))
- Riess A. G., et al., 1998, *Astron. J.*, **116**, 1009
- Rodriguez A. C., Kacprzak T., Lucchi A., Amara A., Sgier R., Fluri J., Hofmann T., Réfrégier A., 2018, preprint, ([arXiv:1801.09070](https://arxiv.org/abs/1801.09070))
- Roncarelli M., Baldi M., Villaescusa-Navarro F., 2018, *MNRAS*, **481**, 2497
- Rumelhart D. E., Hinton G. E., Williams R. J., 1986, *Nature*, **323**, 533
- Schäfer B. M., Heisenberg L., Kalovidouris A. F., Bacon D. J., 2012, *MNRAS*, **420**, 455
- Schmidt B. P., et al., 1998, *Astrophys.J.*, **507**, 46
- Schneider P., 1996, *MNRAS*, **283**, 837
- Schneider P., van Waerbeke L., Jain B., Kruse G., 1998, *MNRAS*, **296**, 873
- Shamir L., Orlov N., Eckley D. M., Macura T., Johnston J., Goldberg I., 2008, *Source Code for Biology and Medicine*, **3**, 13
- Shamir L., Delaney J., Orlov N., Eckley D., Goldberg I., 2010, *PLoS Comput Biol* **6**(11): e1000974
- Shan H., et al., 2018, *MNRAS*, **474**, 1116
- Shirasaki M., Nishimichi T., Li B., Higuchi Y., 2017, *MNRAS*, **466**, 2402
- Simonyan K., Zisserman A., 2014, preprint, ([arXiv:1409.1556](https://arxiv.org/abs/1409.1556))
- Simonyan K., Vedaldi A., Zisserman A., 2013, preprint, ([arXiv:1312.6034](https://arxiv.org/abs/1312.6034))
- Spergel D., et al., 2015, ArXiv e-prints 1503.03757,
- Springel V., 2005, *Mon. Not. Roy. Astron. Soc.*, **364**, 1105
- Springel V., et al., 2005, *Nature*, **435**, 629
- Springenberg J. T., Dosovitskiy A., Brox T., Riedmiller M., 2014, preprint, ([arXiv:1412.6806](https://arxiv.org/abs/1412.6806))
- Springer O. M., Ofek E. O., Weiss Y., Merten J., 2018, preprint, ([arXiv:1808.07491](https://arxiv.org/abs/1808.07491))
- Srivastava N., Hinton G., Krizhevsky A., Sutskever I., Salakhutdinov R., 2014, *Journal of Machine Learning Research*, **15**, 1929
- Szegedy C., Zaremba W., Sutskever I., Bruna J., Erhan D., Goodfellow I., Fergus R., 2013, preprint, ([arXiv:1312.6199](https://arxiv.org/abs/1312.6199))
- Szegedy C., et al., 2014, CoRR, abs/1409.4842
- Szegedy C., Ioffe S., Vanhoucke V., 2016, CoRR, abs/1602.07261
- Tamura H., Mori S., Yamawaki T., 1978, *IEEE Transactions on Systems, Man, and Cybernetics*, **8**, 460
- Teague M. R., 1980, *J. Opt. Soc. Am.*, **70**, 920
- Tessore N., Winther H. A., Metcalf R. B., Ferreira P. G., Giocoli C., 2015, *J. Cosmology Astropart. Phys.*, **10**, 036
- Troxel M. A., et al., 2018, *Phys. Rev. D*, **98**, 043528
- Van Waerbeke L., et al., 2013, *MNRAS*, **433**, 3373
- Viel M., Haehnelt M. G., Springel V., 2010, *JCAP*, **1006**, 015
- Vikhlinin A., et al., 2009, *ApJ*, **692**, 1060
- Villaescusa-Navarro F., Banerjee A., Dalal N., Castorina E., Scoccimarro R., Angulo R., Spergel D. N., 2017, preprint, ([arXiv:1708.01154](https://arxiv.org/abs/1708.01154))
- White S. D. M., 1993, in Gleiser R. J., Kozameh C. N., Moreschi O. M., eds, *General Relativity and Gravitation 1992*. pp 331–+
- White S. D. M., 1996, in Schaeffer R., Silk J., Spiro M., Zinn-Justin J., eds, *Cosmology and Large Scale Structure*. p. 349
- White S. D. M., Rees M. J., 1978, *MNRAS*, **183**, 341
- Winther H. A., et al., 2015, *Mon. Not. Roy. Astron. Soc.*, **454**, 4208
- Wright B. S., Winther H. A., Koyama K., 2017, *J. Cosmology Astropart. Phys.*, **10**, 054
- Wu C.-M., Chen Y.-C., Hsieh K.-S., 1992, *IEEE Transactions on*

- [Medical Imaging](#), 11, 141
 Wu Y., et al., 2016, CoRR, abs/1609.08144
 Zeiler M. D., Fergus R., 2013, preprint, ([arXiv:1311.2901](#))
 Zennaro M., Bel J., Villaescusa-Navarro F., Carbone C., Sebusatti E., Guzzo L., 2017, *MNRAS*, 466, 3244
 Zernike v. F., 1934, *Physica*, 1, 689

APPENDIX A: WND-CHARM FEATURES

The total length of the `wnd-charm` feature vector entails 2919 descriptors, which can be divided into five families. We provide an overview of the features and their respective families in table A1. The algorithm does not only work on the image itself (raw), but also on its Fourier (F), Wavelet (W), Chebyshev (C) or Edge transformation (E) as indicated by the 'Input' column of table A1. Transformations of transformations are considered by the bracket notation. While Fourier and Chebyshev transforms are implemented using common algorithms and methodologies, the Wavelet transformation is performed with a one level filter pass with a 5th order symlet (Orlov et al. 2008) and the Edge transformation is carried out using a Prewitt operator (Prewitt 1970) to approximate the image gradient.

The pixel statistics family is made out of four different subclasses, with the simplest being the intensity statistics consisting of mean, median, standard deviation, minimum and maximum. The multi-scale histograms are calculated by using three, five, seven or nine bins to order the pixel amplitudes. The counts in each of those bins makes up the 24 features in this subclass. The combined moments are mean, standard deviation, skewness and kurtosis, which are calculated in a horizontal stripe through the image centre and with a width which is half the total image width. The stripe is then rotated by 45, 90 and 135 degrees and the measurement is repeated. Those 16 numbers are sampled into three bins each, providing a total of 48 features. The Gini coefficient (Abraham et al. 2003) is a measure of how equal the spectrum of pixel intensities is distributed within the image.

The second feature family is comprised of polynomial decompositions. The coefficients of an order 20 Chebyshev and an order 23 Chebyshev-Fourier (Orlov et al. 2006) transformation are sorted into 32 bin histograms. Radon transformations are carried out along lines with an inclination angle of 0, 45, 90 and 135 degrees with respect to the image horizontal (Radon 1917) and ordered in 3 bin histograms. The class of Zernike coefficients is derived from a 2D Zernike decomposition of the image (Teague 1980) and the first 72 of those coefficients contribute to the feature vector.

The use of textures is common in image processing and is a way of describing spatial correlations of intensity values. We extract seven Gabor filters (e.g. Fogel & Sagi 1989) using Gaussian harmonic functions and define their image occupation area as a feature. Tamura textures are described in detail in Tamura et al. (1978) and `wnd-charm` uses contrast, directionality, coarseness sum and coarseness binned into a 3 sample histogram. The 28 Haralick textures are specific properties of the grey-level dependence matrix of the image and are described in Haralick et al. (1973). The fractal analysis is based on a Brownian motion model of the image following Wu et al. (1992) and `wnd-charm` uses the first 20 parameters of this analysis as features.

Object statistics are only derived from the raw image data. The starting point is an edge transform using a Prewitt filter and mean, median, variance and 8-bin histogram of both image gradient and its directionality add up to 22 features, which are supplemented by the total number of edge pixels, their genus and the differences between the directionality bins. Otsu features and their inverse are calculated after the application of an Otsu threshold (Otsu 1979). Finally, for all objects the algorithm calculates minimum, maximum, mean, median, variance and 10-bin histogram for area and image-centre distance of all Otsu objects in the image.

APPENDIX B: DEEP NEURAL NETWORKS

In this appendix we collect some more detailed information about deep neural networks. The first section formally defines all network layers used in this work and the second section deals with activation functions. The third section provides a thorough description about the architecture of the convolutional neural network (CNN) that we use in our analyses.

B1 Layers

Given a 2D input vector I_{ijc} with $\#I_{ijc} = (X, Y, l)$ a convolution layer applies the following operation to produce an output O_{ijc}

$$\text{Conv}(n, m, \Delta i, \Delta j, p, C) I_{i'j'c'} = O_{ijc} \quad (\text{B1})$$

$$O_{ijc} = B_c + \sum_{i'=1}^n \sum_{j'=1}^m \sum_{c'=1}^l W_{i'j'c'}^c I_{(i\Delta i+i')(j\Delta j+j')c'} \quad (\text{B2})$$

$$w_{\text{conv}} = \{B_c, W_{ijc}\} \quad \forall c \quad (\text{B3})$$

$$\#O_{ijc} = \left(\frac{X}{\Delta i}, \frac{Y}{\Delta j}, l \right) \quad \text{for } p = s \quad (\text{B4})$$

$$\#O_{xyc} = \left(\frac{X}{\Delta i} - \frac{n}{2}, \frac{Y}{\Delta j} - \frac{m}{2}, C \right) \quad \text{for } p = v. \quad (\text{B5})$$

The stride parameters Δi and Δj allow one to implement dimensional reduction. The parameter p indicates if the input data is padded, which means that additional rows and columns are added in order to produce an output which has exactly the same spatial shape as the input, at least in the absence of stride. This is known as *same* padding $p = s$. Alternatively the data can stay unaltered, or *valid* $p = v$, which means that the spatial dimensions of the data vector are slightly reduced, since every convolution must be fully contained within the 2D image domain.

We use four different kinds of pooling layers. Their main functionality is either an averaging

$$\text{AvgPool}(n, m, \Delta i, \Delta j, p) I_{i'j'c} = O_{ijc} \quad (\text{B6})$$

$$O_{ijc} = \frac{1}{nm} \sum_{i'=1}^n \sum_{j'=1}^m I_{(i\Delta i+i')(j\Delta j+j')c} \quad (\text{B7})$$

$$\#O_{ijc} = \left(\frac{X}{\Delta i}, \frac{Y}{\Delta j}, C \right) \quad \text{for } p = s \quad (\text{B8})$$

$$\#O_{ijc} = \left(\frac{X}{\Delta i} - \frac{n}{2}, \frac{Y}{\Delta j} - \frac{m}{2}, l \right) \quad \text{for } p = v, \quad (\text{B9})$$

Family	Class	Features	Input	Reference
Pixel statistics	Combined moments	48	raw, F, W, C, C(F), W(F) F(W), F(C), C(W), E, F(E), W(E)	–
	Gini coefficient	1	raw, F, W, C, C(F), W(F)	Abraham et al. (2003)
	Multiscale histograms	24	F(W), F(C), C(W), E, F(E), W(E) raw, F, W, C, C(F), W(F)	–
	Pixel intensity statistics	5	F(W), F(C), C(W), E, F(E), W(E) raw, F, W, C, C(F), W(F)	–
Polynomial decomposition	Chebyshev coefficients	32	raw, F, W, C, F(W), E, F(E), W(E)	–
	Chebyshev-Fourier coefficients	32	raw, F, W, C, F(W), E, F(E), W(E)	Orlov et al. (2006)
	Radon coefficients	12	raw, F, W, C, C(F), W(F) F(W), F(C), C(W), E, F(E), W(E)	Radon (1917)
	Zernike coefficients	72	raw, F, W, C, F(W), E, F(E), W(E)	Teague (1980))
Textures	Fractal analysis	20	raw, F, W, C, C(F), W(F) F(W), F(C), C(W), E, F(E), W(E)	Wu et al. (1992)
	Gabor	7	raw	Fogel & Sagi (1989)
	Haralick	28	raw, F, W, C, C(F), W(F) F(W), F(C), C(W), E, F(E), W(E)	Haralick et al. (1973)
	Tamura	6	raw, F, W, C, C(F), W(F) F(W), F(C), C(W), E, F(E), W(E)	Tamura et al. (1978)
Objects	Edge features	28	raw	Prewitt (1970)
	Otsu object features	34	raw	Otsu (1979)
	Inverse Otsu object features	34	raw	Otsu (1979)

Table A1. `wnd-charm` image features used in this analysis.

or a maximum selection operation

$$\text{MaxPool}(n, m)I_{i'j'c} = O_{ijc} \quad (\text{B10})$$

$$O_{ijc} = \max \{I_{(i\Delta i + i')(j\Delta j + j')c}\}_{i'=1, j'=1}^{n, m} \quad (\text{B11})$$

$$\#O_{ijc} = \left(\frac{X}{\Delta i}, \frac{Y}{\Delta j}, l \right) \quad \text{for } p = s \quad (\text{B12})$$

$$\#O_{ijc} = \left(\frac{X}{\Delta i} - \frac{n}{2}, \frac{Y}{\Delta j} - \frac{m}{2}, l \right) \quad \text{for } p = v. \quad (\text{B13})$$

Both pooling layers exist also as global versions, indicated by GlobalMaxPool and GlobalAvgPool, where all entries in a channel are considered for either the maximum or averaging operation. In this case the shape of the output reduces to $(1, 1, l)$.

A concatenation layer performs a stacking operation along the c -axis, which means that the spatial dimensionality of each input I_{ijc} must be the same (X, Y).

$$\text{Concatenate}(I_{ijc_1}, \dots, I_{ijc_n}) = O_{ijc} \quad (\text{B14})$$

$$O_{ijc} = I_{ijc_1} \oplus \dots \oplus I_{ijc_n} \quad (\text{B15})$$

$$\#O_{ijc} = (X, Y, C_1 + \dots + C_n), \quad (\text{B16})$$

where the \oplus operator implements the channel stacking. The respective number of input channels is C_1, \dots, C_n for a concatenation of n layers.

Fully-connected, sometimes called affine, layers create a linear mapping between the input and the output

$$\text{FC}(n)I_{ijc'} = O_{ijc} \quad (\text{B17})$$

$$O_{ijc'} = B_{ij} + \sum_{k=1}^X A_{c'k} I_{ijk} \quad (\text{B18})$$

$$w_{\text{FC}} = \{B_{ij}, A_{c'k}\} \quad (\text{B19})$$

$$\#O_{ij} = (1, 1, n). \quad (\text{B20})$$

Here, we assume that the input layer has a simple 1D shape $(1, 1, X)$.

B2 Activation functions

We use three kinds of activation functions. Feature extraction layers such as convolution and pooling layers are often followed by rectangular linear units (ReLU) or its generalisation which is commonly called a leaky rectangular linear unit

$$\text{ReLU}(x) = \max(0, x) \quad (\text{B21})$$

$$\text{leakyReLU}(x; \alpha) = \begin{cases} x & x \geq 0 \\ \alpha x & \text{otherwise.} \end{cases} \quad (\text{B22})$$

The last fully connected layer in a neural network that is used for classification is often followed by softmax function in order to produce predictions in the final output of the network

$$\text{Softmax}(x)_n = \frac{\exp x_n}{\sum_{j=1}^N \exp x_j} \quad \text{for } n = 1, \dots, N. \quad (\text{B23})$$

B3 CNN architecture

In section 4.3 we described the global structure of our CNN, which is largely based on Szegedy et al. (2016). Here we describe in detail the purpose of each of the functional elements that are shown in table 6. After three conventional 3×3 convolutions for initial feature extraction and dimensional reduction, we enter the StemInception layer, which is shown in detail in figure B1. In our CNN, the purpose of the stem layer is twofold. Firstly, it further reduces the data

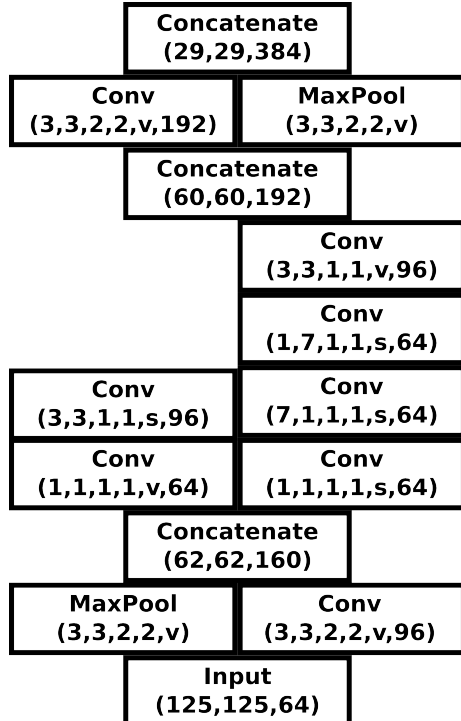


Figure B1. The internal structure of the stem Inception layer. The layout is identical to Szegedy et al. (2016), but with the image dimensions of our mass maps.

vector from 125×125 pixels down to 29×29 pixels, which is a computationally manageable size for applying a large number of convolution channels. Secondly, it already applies a more refined combination of 3×3 , 7×7 and 1×1 convolutions. The latter only have the purpose of channel reduction as explained in Szegedy et al. (2016). The stem layer is followed by the three main inception layers A, B and C. The main purpose of those layers is feature extraction, with a particularly large number of convolutions of varying kernel size. Between the main feature extraction layers we insert reduction layers, breaking the image up further into smaller postage stamps and allowing the application of a larger number of convolution channels within acceptable runtimes and within the memory constraints of the hardware we deploy. The very last concatenation layer of InceptionC is followed by a global averaging layer and a single fully connected layer for classification.

The ReductionA layer, shown in figure B3, consists of a relatively simple combination of 3×3 convolutions and a MaxPooling layer. The purpose of this network module is to reduce the spatial dimension of the images from 29×29 pixels down to 14×14 in order to allow for large convolutions in the following InceptionB layer, which is shown in figure B4. This module consists of larger 7×7 convolutions, split into perpendicular stripes for runtimes reasons and hence makes an important contribution in the feature extraction process. Reduction layer B, shown in figure B5 and reduces the image dimensionality further from 14×14 to 6×16 with a rather complicated combination of convolutions. It is followed by the final InceptionC layer shown in figure B6, which naturally applies only small convolution but using a particularly large amount of channels.

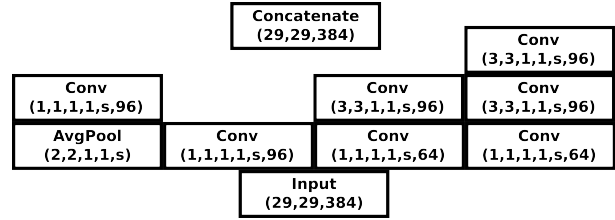


Figure B2. InceptionA layer of our CNN, based on Szegedy et al. (2016).

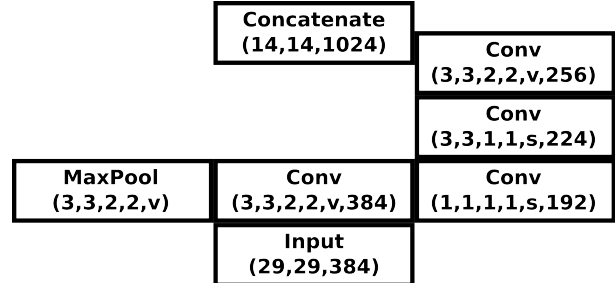


Figure B3. ReductionA layer of our CNN, based on Szegedy et al. (2016).

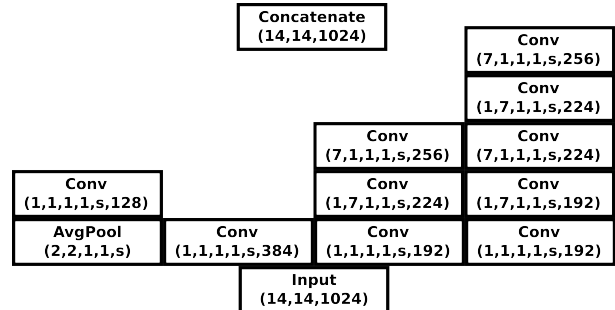


Figure B4. InceptionB layer of our CNN, based on Szegedy et al. (2016).

This paper has been typeset from a Te_X/L_AT_EX file prepared by the author.

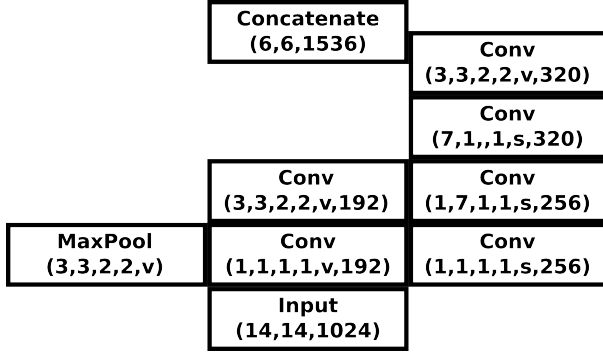


Figure B5. ReductionB layer of our CNN, based on Szegedy et al. (2016).

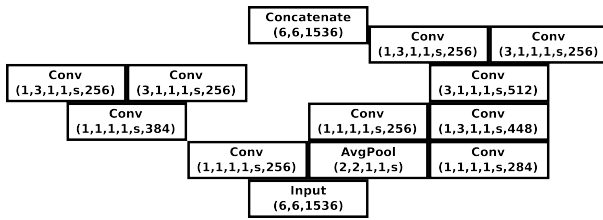


Figure B6. InceptionC layer of our CNN, based on Szegedy et al. (2016).